ORNL/CON-100

OAK RIDGE NATIONAL LABORATORY

UNION CARBIDE

Laboratory Test of a Residential Low-Temperature Water Source Heat Pump

V. C. Mei

OPERATED BY
UNION CARBIDE CORPORATION
FOR THE UNITED STATES
DEPARTMENT OF ENERGY

Printed [illegible]

[illegible]

NTIS [illegible]

[illegible]

manufactur[illegible]

endorsement [illegible]

any agency [illegible]

necessar[illegible]

thereof.

ORNL/CON-100

Energy Division

LABORATORY TEST OF A RESIDENTIAL LOW-TEMPERATURE WATER SOURCE HEAT PUMP

V. C. Mei

Date Published: April 1984

Prepared by the
OAK RIDGE NATIONAL LABORATORY
Oak Ridge, Tennessee 37830
operated by
UNION CARBIDE CORPORATION
for the
U.S. DEPARTMENT OF ENERGY
under Contract No. W-7405-eng-26

CONTENTS

LIST OF FIGURES

LIST OF TABLES

ACKNOWLEDGMENTS

The author would like to thank D. E. Holt, who is responsible for the construction of the heat pump test stand, and J. T. Farmer, who built the refrigerant system and maintained it throughout the experiment. Thanks are due W. W. Smith for the system's electrical wiring.

The author is grateful to R. D. Ellison, C. K. Rice, and W. A. Miller for their many useful discussions during the test. C. K. Rice also provided the sample calculation for the application of the test results.

The author appreciates the assistance provided by S. T. Ball in setting up the instrumentation of the test stand.

ABSTRACT

A residential unitary low-temperature water source heat pump was tested in the laboratory. Tests were performed over a broad range of source water temperatures, 7.2 to 21.1°C (45.0 to 70.0°F), and water flow rates, 3.2×10^{-4} to 8.2×10^{-4} m^3/s (5 to 13 gpm).

The heat pump capacity and coefficient of performance (COP) were found to be linearly related to the source water temperatures. In the heating mode, both the capacity and COP increased with increasing source water temperature and water flow rate. However, when an assumed water pumping power for a 46-m total head was taken into account in the COP calculation, the net COP for both heating and cooling decreased with increasing water flow rate.

For cyclic operation over the tested source water temperature range, the coefficient of degradation, C_D, ranged from 0.196 to 0.137 for heating and from 0.131 to 0.161 for cooling. The effect of inlet air humidity was also studied for cooling mode operation.

A sample calculation is included to demonstrate the application of the test results in calculating the annual performance factor. The test results are used to form a data base on the performance of a typical residential unitary low-temperature water source heat pump.

1. INTRODUCTION

Groundwater temperatures in the continental United States range from about 5.6°C (42.0°F) in the northernmost regions to about 25.6°C (78.0°F) in the Deep South. This water provides an ideal heat source or sink for heating and cooling with water source heat pumps. Since the groundwater temperature at any location stays almost constant year round, regardless of the extremes of the ambient air temperature, a properly designed groundwater heat pump system will operate at a higher seasonal performance factor than an air-to-air unit in the same climate. However, in the past the expense of drilling wells had limited such systems to those areas where abundant, moderate-temperature groundwater was available at moderate depths.

In recent years, escalating energy costs have brought about a search for more energy-efficient ways of residential space heating and air conditioning. It is apparent that groundwater heat pumps can provide significant energy savings, and the old idea of using groundwater-coupled heat pumps is now becoming a promising prospect for energy conservation. Many water source heat pumps are now designed to operate with relatively cold groundwater, as low as 4.4°C (40.0°F), which considerably extends their geographic range of applicability. Although low-temperature groundwater heat pumps have become more popular, well-instrumented test data are still quantitatively inadequate. The purpose of this study is to collect sufficient information to form a data base on the performance of such a typical residential, unitary low-temperature water source heat pump.

The experiment described in this report can be divided into four parts: steady-state and cyclic operations for both heating and cooling modes. For steady-state operation, the tests were performed with inlet water temperature and flow rate as parameters. In addition, the effect of inlet air moisture content on the heat pump performance was tested for steady-state cooling operation.

For cycling tests, the cycling loss, which is caused by refrigerant migration from the high- to low-pressure side during the off-cycle, was experimentally determined with water inlet temperature and water flow rate as parameters. For cooling mode cycling tests, both dry- and wet-coil tests were performed, under certain operating conditions, to confirm that cycling loss was independent of inlet air humidity, as concluded by Didion and Kelly.[1]

To estimate the annual performance factor (APF), the degradation coefficient, C_D, was calculated with water inlet temperature and water flow rate as parameters. Finally, an example of estimating the APF for a house with known heating and cooling load is presented to demonstrate the application of the test data.

2. DISCUSSION AND CONCLUSIONS

For both heating and cooling, the capacity and coefficient of performance (COP) of the tested heat pump are linear functions of inlet water temperature over the tested range of 7.2 to 21.1°C (45.0 to 70.0°F).

The steady-state heating capacity and COP increased with increasing inlet water temperature and flow rate if the water circulating pump power was not considered. The steady-state cooling capacity and COP decreased with increasing entering water temperature and increased with increasing water flow rate, although the effect of the water flow rate on the capacity and COP was very small.

For both heating and cooling steady-state COP calculation, if we added the water pump power input, assuming a total head of 46 m (150 ft) and a pump-motor efficiency of 0.3, to the heat pump power input, the COP decreased with increasing water flow rate.

For cooling mode steady-state operation, the increase of inlet air humidity increased the heat pump total capacity but decreased the sensible capacity output.

Both heating and cooling mode cycling tests were performed on a 6-min-on and 24-min-off time schedule. For heating mode cyclic operation, the cycling loss decreased from 16.5 to 11.3% with an increase of entering water temperature from 7.2°C (45.0°F) to 21.1°C (70.0°F). The degradation coefficient was from 0.196 to 0.137 over the same water temperature range. For cooling mode cyclic operation, both dry- and wet-coil tests were performed at a constant entering water temperature and flow rate. The results indicate that the cycling loss is independent of the humidity of the entering air. The cooling mode cycling loss increased from 10.7 to 13.4% with an increase of the entering water temperature from 7.2°C (45.0°F) to 21.1°C (70.0°F). The degradation coefficient varied from 0.132 to 0.161 over the same water temperature range. The degradation factors are smaller than air to air heat pumps.

The cycling loss and degradation coefficients, for both heating and cooling mode operation, were independent of water flow rate.

The effect on heat pump performance of extra refrigerant added to the system cannot be easily checked. For steady-state operation, the test data were compared with the manufacturer's published information and were found to be very close. Therefore, it is reasonable to assume that the effect of extra refrigerant charging is negligible. However, such a comparison for cyclic operation cannot be made because of the effect of the refrigerant migration. The effect of refrigerant charging will be incorporated in future reports when further testing is completed.

3. DESCRIPTION OF TEST UNIT

The heat pump tested is of a commercially available unitary design; an air handling compartment is located above another compartment containing the compressor and the water-to-refrigerant heat exchanger. The two compartments are separated by an insulated panel. The manufacturer's rated heating and cooling capacities for the unit are 11.1 kW (37,800 Btu/h) and 10.0 kW (34,100 Btu/h), respectively, at 12.8°C (55.0°F) inlet water temperature.

The compressor has a nominal rating of 1.9 kW (2.5 hp) using R-22 as the refrigerant. The blower of the air handling system, with a three-speed, 0.37-kW (0.5-hp) motor, is rated at 7.1×10^{-1} m^3/s (1500 ft^3/min) at 24.7 Pa (0.1 in. water) of external pressure.

Refrigerant flow in both the heating and cooling modes is controlled by a single thermostatic expansion valve; the temperature sensing bulb is on the compressor suction line. The refrigerant charge recommended by the manufacturer is 1.6 kg (3.5 lb). However, extra copper tubing was added to the system for installation of the instruments to measure refrigerant flow rate and pressure, which increased the total volume of the refrigerant system. Therefore, an additional 1.6 kg (3.6 lb) of R-22 was added to the system so that the heat pump steady-state heating output was close to that given in the manufacturer's published data.

The water-to-refrigerant heat exchanger has a coaxial tube-in-tube design, with a helical fluted inner tube to enhance the flow turbulence and heat transfer area. Refrigerant flows in the annulus area and water flows in the inner tube. An external water circulation pump was installed to circulate the water through the heat exchanger. This pump would normally be the well pump in a residential installation.

4. DESCRIPTION OF TEST APPARATUS

The test apparatus measures both air- and refrigerant-side energy changes across the air-to-refrigerant heat exchanger, water and refrigerant energy changes across the water-to-refrigerant heat exchanger, and power consumption of the compressor and blower motors. Figure 1 shows the refrigerant and water circulating loops and the location of pressure and temperature sensors and turbine meters.

A "bootstrap" air loop was built around the heat pump air handling compartment (Fig. 2) to provide control over the inlet air temperature by recirculating part of the air leaving the heat pump.

Air flow rate was determined by a duct air monitor that has a cross section of 0.092 m^2 (1.00 ft^2). The device measured the average velocity head of the inlet air. A low-pressure differential transducer converted the velocity head into direct-current voltage as an input signal to the data acquisition system (DAS) for air velocity calculation. Average air temperatures entering and leaving the unit were measured by two sets of nine thermocouples connected in parallel. Two humidity sensors measured the inlet and outlet air relative humidities for heating mode tests; two single thermocouples covered with wetted wicks measured wet-bulb temperatures of entering and exiting air for cooling mode tests.

The refrigerant flow rate was measured by a turbine flowmeter connected in series with a rotameter, which also served as a sight glass. The refrigerant pressure drops across the air-to-refrigerant and water-to-refrigerant heat exchangers were measured by four pressure transducers. The refrigerant temperatures at various locations shown in Fig. 1 were measured by single thermocouples clamped on the refrigerant lines and covered with insulation. Pressure gages made it possible to visually check the pressures on the compressor suction and discharge lines as well as the pressures before and after the expansion valve.

The water flow rate was measured by a turbine flowmeter connected in series with a rotameter. The inlet and outlet water temperatures were measured by single thermocouples in wells installed at the inlet and outlet of water line fittings.

Water was taken from a 3.8-m^3 (1000-gal) insulated tank that was equipped with an ice maker and was capable of chilling the water to 0°C (32.0°F). The heat pump compressor power and blower power consumption are measured by two thermal-watt converters that produced d-c signals proportional to the instantaneous power consumption.

A steam line was installed near the air intake duct to provide humidification when required. A small steam coil, which could raise the inlet air temperature by 1.4°C (2.5°F), was installed in the intake air ductwork to provide fine adjustment of the intake air temperature.

Thermocouples were used for all the temperature measurements. The National Bureau of Standards (NBS) temperature vs millivolt relationship, which was coded into the DAS, could easily be approximated to within 0.11°C (0.20°F), with reference junction temperatures between 21.1 and 32.2°C (70.0 and 90.0°F) and thermocouple junction temperatures between −12.2 and 65.6°C (10.0 and 150.0°F).[2]

The DAS used in this experiment consists of a digital computer with 8K-word core memory, an integrating digital voltmeter with an ohms converter, a reed relay scanner, and a floppy disk drive that could store 27K output data per disk. The programs used by the computer were written in a Digital Equipment Corporation (DEC) FOCAL language modified locally to facilitate data acquisition.

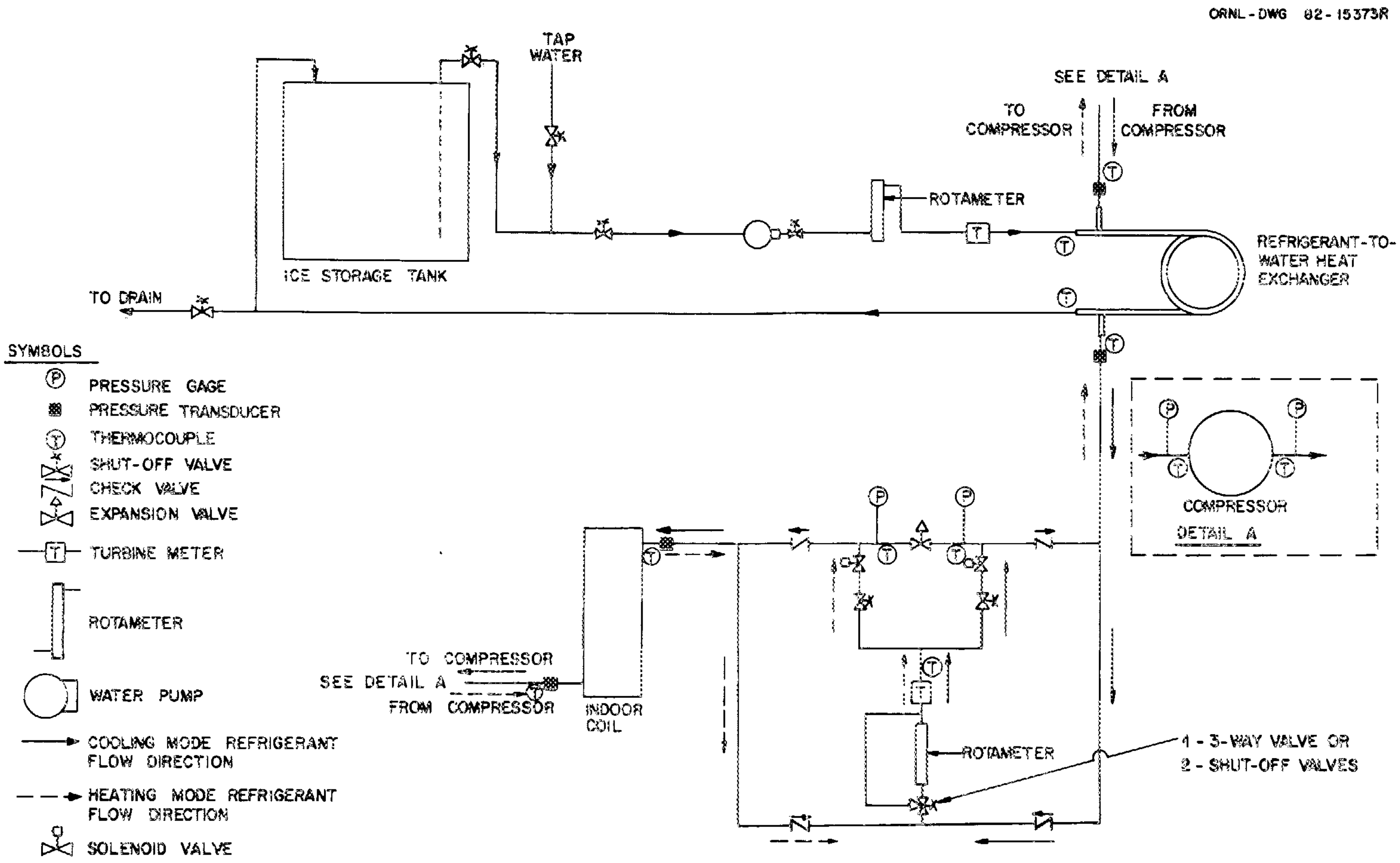

Fig. 1. Schematic of refrigerant and water circulating loops.

ORNL-PHOTO 7120-81

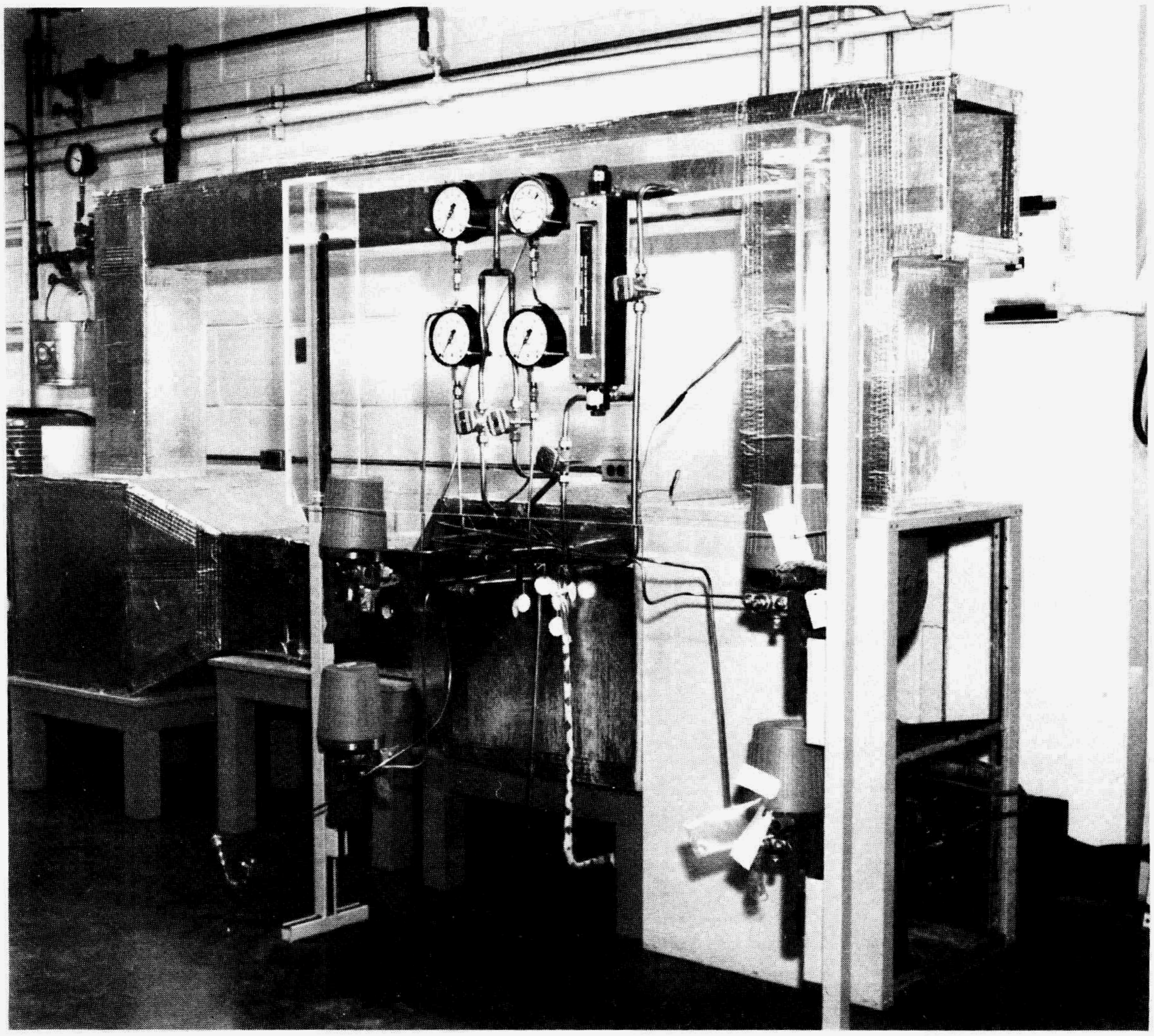

Fig. 2. Air loop arrangement.

The equations used to calculate the thermodynamic properties of the refrigerant, R-22, were developed by Ball[3] from the R-22 property table[4] for a previous heat pump experiment. The air thermodynamic properties were calculated from the equations listed in ref. 5.

5. TEST PROCEDURE

Tests were conducted to study the response of performance parameters to changes in water temperature and flow rate while the heat pump was in operation. The tests were run at water temperatures ranging from 7.2 to 21.1°C (45.0 to 70.0°F) and flow rates ranging from 3.2×10^{-4} to 8.3×10^{-4} m^3/s (5 to 13 gpm).

Because most heat pumps are rated without concern for their water pumping power consumption, we elect to add an assumed pumping power to estimate the system performance. A 4.6-m (150.0-ft) total water head and a pump efficiency of 0.3 were assumed (refer to Fig. 34 for the effect of total head). The pumping power can then be calculated by

$$P_{\text{pump power}} = 0.415 \cdot \dot{m}_w \ , \tag{1}$$

where $\dot{m}_w$ is the water mass flow rate in kilograms per hour and the pump power is in watts.

For refrigerant-side capacity output, the refrigerant enthalpy changes across both heat exchangers are calculated using measured refrigerant pressures and temperatures.

For air-side output, the air enthalpy changes across the heat exchanger are calculated using measured air dry-bulb temperatures and air relative humidities for the heating mode or air wet-bulb temperatures for the cooling mode.

5.1 Heating Mode Steady-State Tests

The water in the storage tank was first heated to about 27°C (80°F), and the heat pump was then operated at a selected water flow rate using water from the storage tank. The water went through the heat exchanger and was recirculated back to the tank. The water temperature in the tank thus decreased slowly, at a rate of about 1°C per 12.5 to 18 min (1°F per 7.0 to 10.0 min). Data collection began when the inlet water temperature reached 21.1°C (70.0°F) and continued until the water inlet temperature dropped below 7.2°C (45.0°F). Since the heat pump had run for at least 1 h before data collection began and since the supply water temperature changed slowly, it is reasonable to assume that the heat pump was tested under quasi-steady-state conditions.

In the comparison of the refrigerant- and air-side energy changes for the air-to-refrigerant heat exchanger, the fan power consumption was added to the refrigerant-side heating capacity.

5.2 Heating Mode Cycling Tests

The cycling tests were performed on a 6-min-on and 24-min-off time schedule for the same water flow rates and temperature range as that specified in Sect. 4.1. The water in the storage tank was first heated to about 4.4°C (8.0°F) above the desired water temperature for the test. The water was allowed to recirculate back to the tank while the heat pump was in operation. By the time the water temperature in the tank dropped to the desired level for the test, the heat pump would already be running in a quasi-steady-state condition. The heat pump system would then be shut off for a period of 24 min and started for a cycling test.

During the 6 min of "on" time, the water that went through the heat exchanger was drained to a sink so that a constant supply water temperature could be maintained. A minimum of four "on" and four "off" cycles were run for each test.

5.3 Cooling Mode Steady-State Tests

In cooling mode operation, the inlet air moisture could strongly affect the heat pump performance because of the dehumidification effect. It was found that the humidity sensors were not accurate enough to collect the data required for the air humidity ratio calculation. Consequently, the wet-bulb temperatures of the inlet and discharge air were measured, together with the dry-bulb temperatures, to calculate the amount of moisture condensed during the operation.

To start the test, the water in the storage tank was first chilled to about 3.3°C (38.0°F). The water that went through the heat exchanger was allowed to recirculate back to the tank. Data collection began when the inlet water temperature reached 7.2°C (45.0°F) and terminated when the inlet water temperature reached 21.1°C (70.0°F). The inlet air dry- and wet-bulb temperatures were maintained at 26.7 ± 0.3°C (80.0 ± 0.5°F) and 17.2 ± 0.3°C (63.0 ± 0.5°F) respectively. When the refrigerant- and air-side energy changes were compared, the blower power consumption was subtracted from the refrigerant-side cooling capacity. Refrigerant- and water-side energy changes across the water-to-refrigerant heat exchanger were also calculated.

5.4 Cooling Mode Cycling Tests

The procedure used was similar to that for the heating mode cycling tests, described in Sect. 4.2, except that the water in the storage tank was first chilled to 4.4°C (8.0°F) below the desired test water temperature. However, because of the heat pump cycling, the response of the air inlet wet-bulb temperature measurement was too slow at the beginning of the "on" cycle. It was assumed that the inlet air humidity ratio was constant. Given the air dry-bulb temperature and air humidity ratio, the air thermodynamic properties could be calculated. Tests were performed for water flow rates of 3.2×10^{-4} and 8.2×10^{-4} m^3/s (5.0 and 13.0 gpm) only and for water temperatures ranging from 7.2 to 21.1°C (45.0 to 70.0°F). The inlet air was maintained at 26.7 ± 0.3°C (80.0 ± 0.5°F) dry bulb. Didion and Kelly[1] reported that the following relationship exists for cooling mode cycling tests:

$$\frac{(\mathrm{COP})_{\mathrm{cyc\ w}}}{(\mathrm{COP})_{\mathrm{ss\ w}}} = \frac{(\mathrm{COP})_{\mathrm{cyc\ D}}}{(\mathrm{COP})_{\mathrm{ss\ D}}}\,, \tag{2}$$

where $(\mathrm{COP})_{\mathrm{cyc\ w}}$, $(\mathrm{COP})_{\mathrm{cyc\ D}}$, $(\mathrm{COP})_{\mathrm{ss\ w}}$, and $(\mathrm{COP})_{\mathrm{ss\ D}}$ represent the heat pump cyclic and steady-state COP of wet and dry coils respectively.

A few cyclic tests were performed, with inlet air humidity ratio as the parameter, at 3.2×10^{-4} m^3/s (5.0 gpm) water flow rate and 12.2°C (54.0°F) water temperature to confirm the above relationship.

5.5 Cooling Mode Steady-State Tests with Inlet Air Humidity as the Parameter

To have a constant-temperature water supply, tap water was used for this test. The heat pump was operated for at least 1 h before the data collection began. Steam was injected into the inlet air while the dry-bulb temperature was maintained at 26.7 ± 0.3°C

(80.0 ± 0.5°F). The heat pump sensible and latent capacities were calculated. The tests were conducted at 3.2×10^{-4} and 5.8×10^{-4} m^3/s (5.0 and 9.0 gpm) water flow rate, with inlet air wet-bulb temperature varying from 12.8 to 21.1°C (55 to 70°F) and water inlet temperature at 12.2°C (54.0°F).

6. HEATING MODE STEADY-STATE AND CYCLIC OPERATION TEST RESULTS

6.1 Heating Mode Steady-State Test Results

6.1.1 Heating Capacity and COP

The heating capacity is defined as the sum of the heat rejected by the coil and the power input to the indoor fan. The COP is defined as the ratio of heating capacity to total power input.

Figure 3 shows the capacity and power input (no pump power) as functions of entering water temperature at 5.7×10^{-4} m^3/s (9.0 gpm) water flow rate. The capacity increased with increasing water temperature from 9.4 kW at 7.2°C (45.0°F) to 12.89 kW at 21.1°C (70.0°F) (from 32,100 to 44,000 Btu/h). The power consumption also increased with increasing water temperature, from 3.1 to 3.7 kW. Figure 4 is the same as Fig. 3 except that the water flow rate is an additional parameter. It shows that the capacity increases with water flow rate. At 12.8°C (55.0°F), the capacity increases from 10.3 kW (35,000 Btu/h) at 3.2×10^{-4} m^3/s (5.0 gpm) to 11.2 kW (38,200 Btu/h) at 8.2×10^{-4} m^3/s (13.0 gpm). The ARI rated COP of the unit is very close to our test result at 21.1°C (70.0°F).

ORNL-DWG 82-15440R

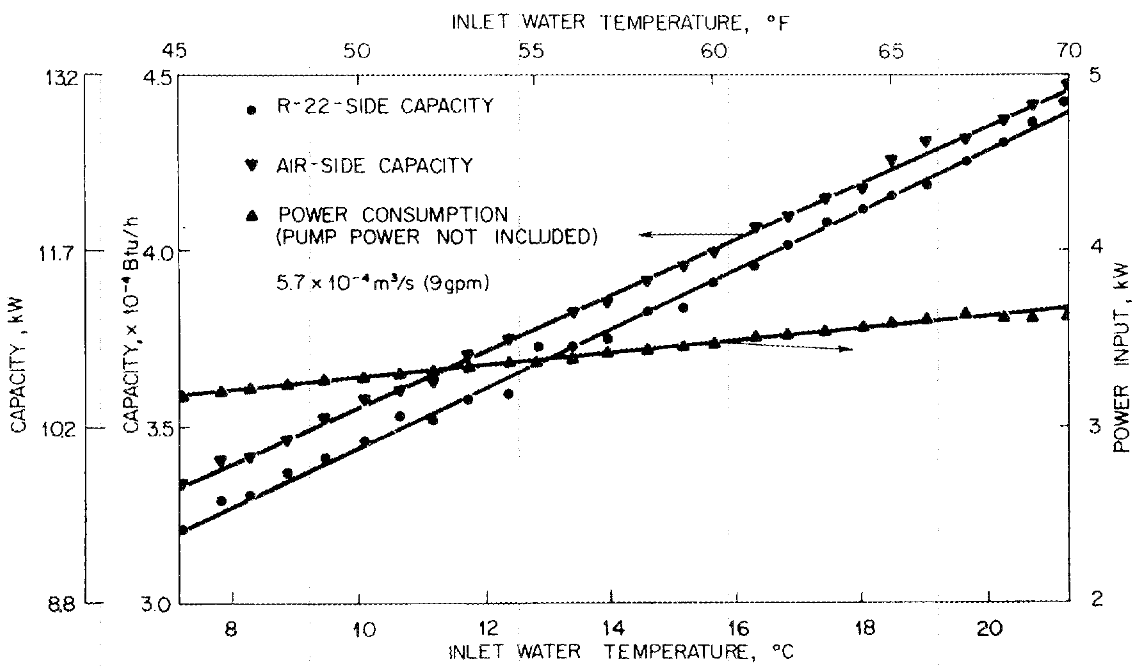

Fig. 3. Heating mode capacity as a function of inlet water temperature at 5.7×10^{-4} m^3/s (9 gpm) water flow rate.

ORNL-DWG 82-15426R2

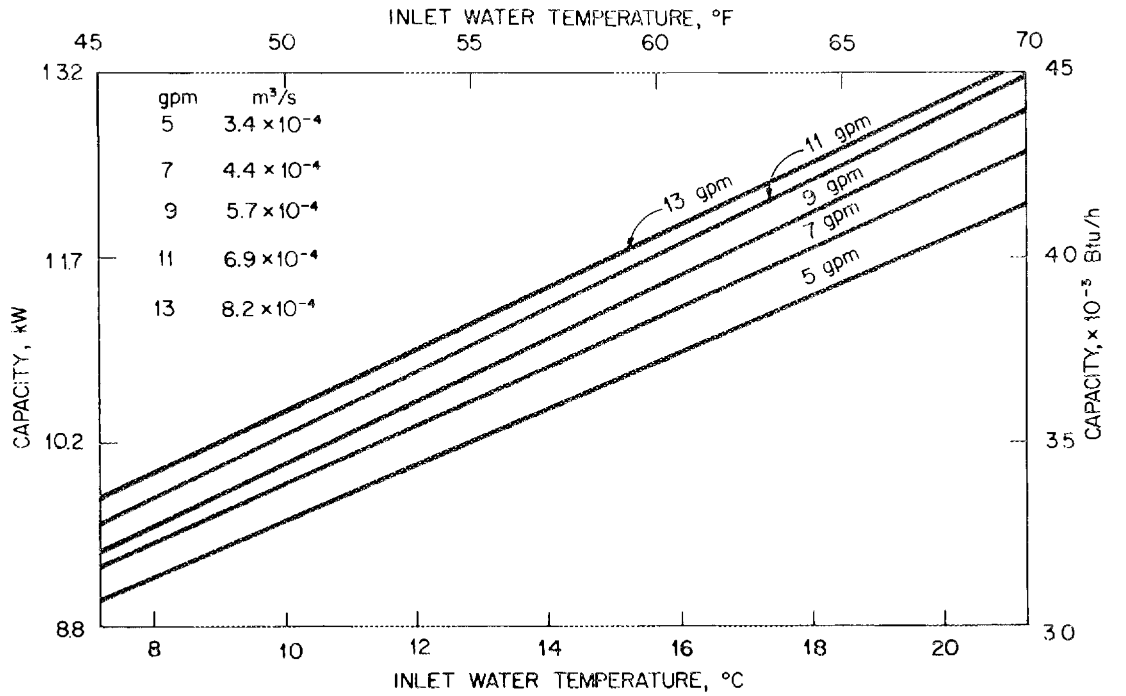

Fig. 4. Heating mode capacity as a function of inlet water temperature and water flow rate.

Figure 5 shows typical test results for COP as a function of entering water temperature at 5.7×10^{-4} m^3/s (9.0 gpm) water flow rate. The COP increased with increasing water temperature from 2.96 to 3.5 (refrigerant side) over the temperature range. Figure 6 shows the COP as a function of entering water temperature with water flow as a parameter. It indicates that the COP increases with increasing water flow rate. For example, the COP at 12.8°C (55.0°F) increases from 3.11 to 3.26 when the flow rate is increased from 3.2×10^{-4} to 8.2×10^{-4} m^3/s (5.0 to 13.0 gpm). Figure 7 is the same as Fig. 6 except that the water pump power input is included in calculating the COP. It shows that the COP decreases with increasing water flow rate. The COP decreases from 2.72 to 2.4 at 12.8°C (55.0°F) entering water temperature when the flow rate is increased from 3.2×10^{-4} to 8.2×10^{-4} m^3/s (5.0 to 13.0 gpm). Figure 7 indicates that, if we wanted to operate the heat pump at a higher COP, we would have to operate it at a lower water flow rate with a slightly reduced heating capacity output if the total water head were 46.0 m (150 ft).

6.1.2 Compressor Operation

The compressor performance parameters for a range of water inlet temperatures at 0.57 m^3/s (9.0 gpm) water flow rate are shown in Table 1. The refrigerant flow rate went up with increasing inlet water temperatures because of the increase of the suction pressure, which increases the density of the refrigerant vapor reaching the compressor. Higher suction pressure causes higher refrigerant flow rate and discharge pressure, which results in better refrigerant condensing because of the higher temperature differential between the inlet room air and discharge gas. The pressure ratio, therefore, decreased with the increase

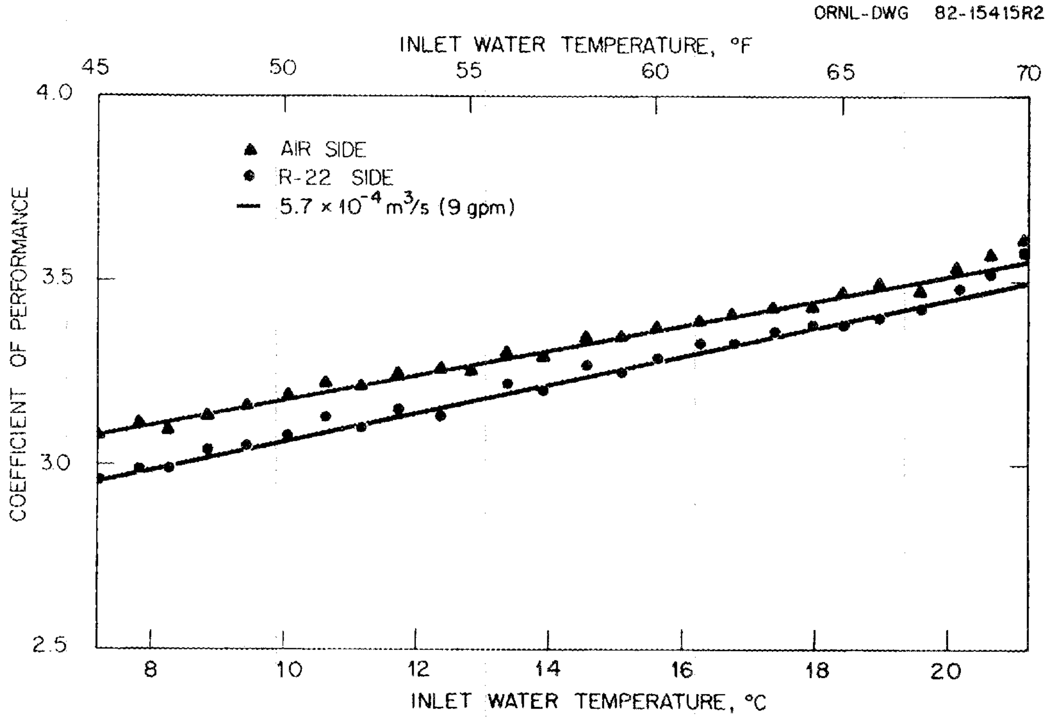

Fig. 5. Heating mode steady-state COP as a function of inlet water temperature at 5.7×10^{-4} m^3/s (9 gpm) water flow rate.

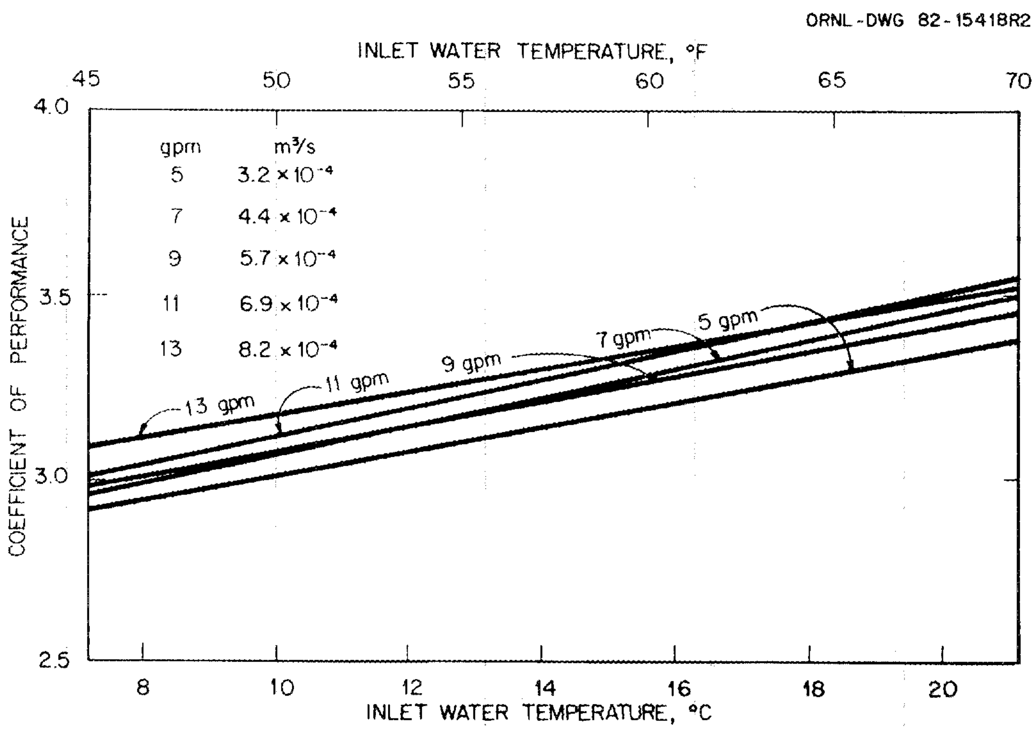

Fig. 6. Heating mode steady-state COP as a function of inlet water temperature and water flow rate.

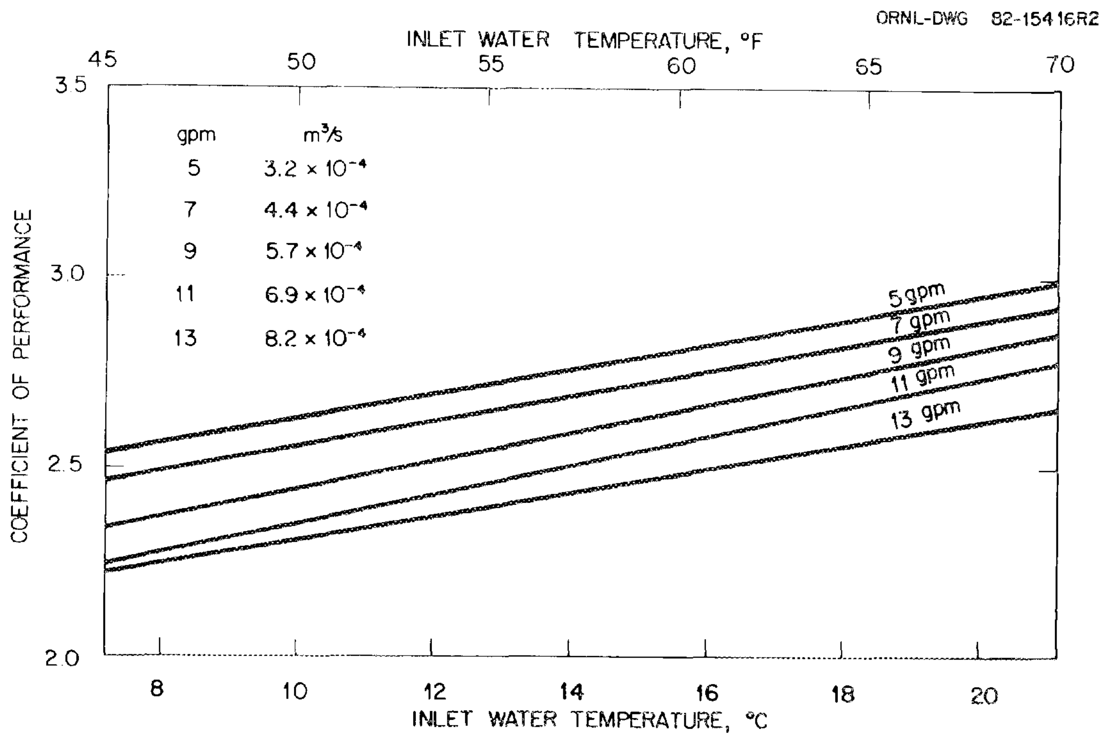

Fig. 7. Heating mode steady-state COP (with water pumping power) as a function of inlet water temperature and water flow rate.

Table 1. Heating mode compressor operating characteristics

Tests performed at 5.7×10^{-4} m^3/s (9.0 gpm) water flow rate

Water inlet temperature		Power input to motor		Refrigerant mass flow rate		Pressure ratio	Combined motor-comp. efficiency[a]	Volumetric efficiency[b]	Degree of superheat	
°C	(°F)	kW	(Btu/h)	kg/h	(lb/h)				°C	(°F)
7.2	(45.0)	2.70	(9,205)	155	(342)	3.42	0.508	0.723	6.2	(11.2)
10.0	(50.0)	2.80	(9,567)	170	(374)	3.29	0.519	0.740	6.7	(12.1)
12.8	(55.0)	2.90	(9,877)	186	(409)	3.18	0.535	0.759	7.2	(12.9)
15.6	(60.0)	3.00	(10,239)	196	(433)	3.08	0.531	0.757	7.8	(14.1)
18.3	(65.0)	3.12	(10,642)	211	(465)	2.98	0.534	0.762	8.4	(15.1)
21.1	(70.0)	3.15	(10,741)	226	(498)	2.80	0.538	0.780	9.6	(17.2)

[a]This efficiency is the ratio of ideal isentropic work (between actual shell inlet conditions of the refrigerant and the discharge pressure) to the electrical power input to the compressor.

[b]Volumetric efficiency is defined as

$$\eta_v = \frac{\dot{m}_{ref}}{\rho_s \, DN} ,$$

where

η_v = volumetric efficiency,
$\dot{m}_{ref}$ = measured refrigerant mass flow rate,
ρ_s = density of refrigerant vapor at hermetic unit shell inlet,
D = compressor displacement (swept volume),
N = compressor speed.

of water temperature due to higher suction pressure and better condensing of the discharged vapor. The combined motor-compressor and volumetric efficiencies also increased with water inlet temperature, even though they were only weak functions of water inlet temperature and seemed independent of water flow rate, as indicated in Fig. 8.

6.1.3 Water-to-Refrigerant Heat Exchanger Performance

For the water source heat pump test, the water-to-refrigerant heat exchanger was probably the most important component that influenced the heat pump performance since the only test parameters were water inlet temperature and water flow rate.

The heat exchanger is a tube-in-tube coaxial coil with a steel outer shell and a cupronickel inner tube spiraled to enhance the heat transfer surface area and to stimulate the flow turbulence. The refrigerant is on the shell side and water is on the tube side. The refrigerant is counterflow to the water for heating operation and flows concurrently with the water for cooling operation.

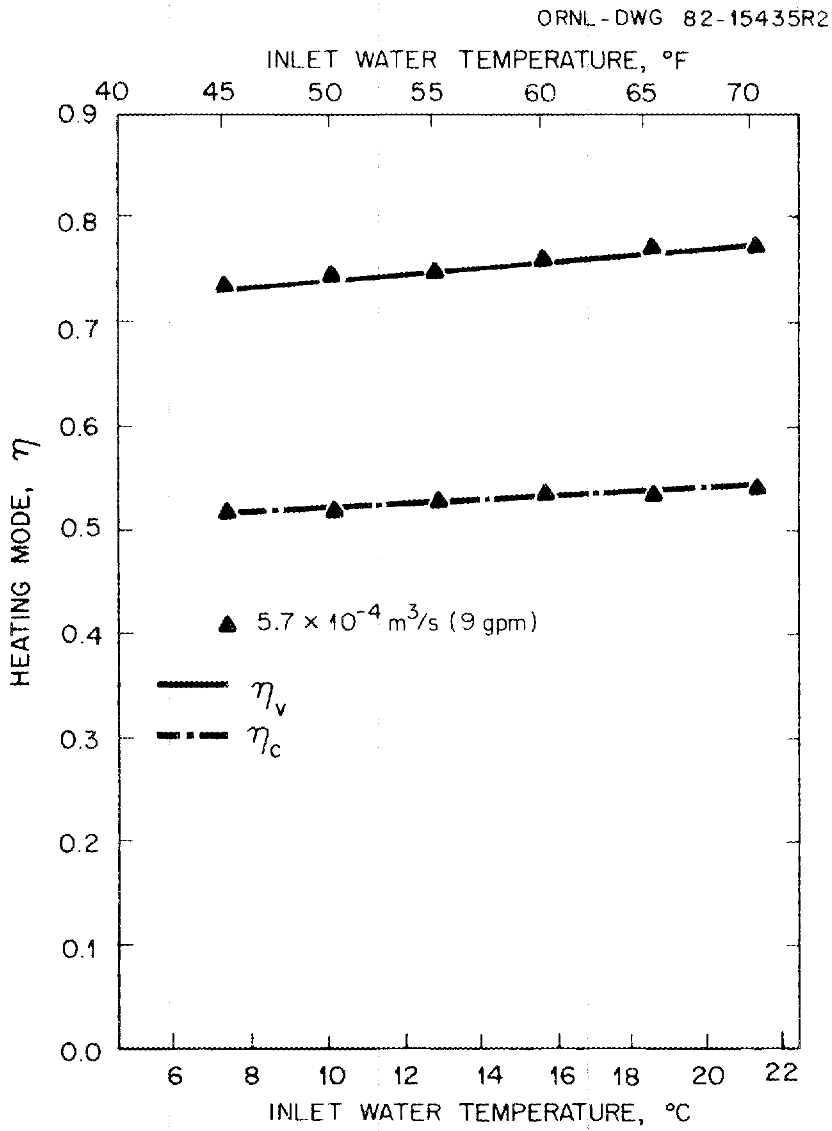

Fig. 8. Heating mode compressor volumetric efficiency (η_v) and combined motor-compressor (η_c) efficiencies as functions of inlet water temperature.

It is difficult to calculate the heat transfer film coefficients on the water and refrigerant sides because of the irregular surface shape and because the refrigerant does not stay in one phase, making calculation of the overall heat transfer coefficient impossible unless the heat exchanger area for each refrigerant region, superheated vapor, two-phase, and subcooled liquid is known. The heat exchanger is not instrumented for detailed analysis in this experiment. However, the parametric studies of the overall heat transfer rate and refrigerant pressure drops were analyzed through the test results.

Figure 9 shows the water-side pressure drop across the exchanger as a function of water flow rate. It shows that, if we double the flow rate from 3.2×10^{-4} to 6.4×10^{-4} m^3/s (5.0 to 10.0 gpm), the pressure drop quadruples. Since the water pump power consumption is an important factor in determining the heat pump COP (Sect. 6.1.1), the water-side pressure drop can seriously decrease the system performance at a high water flow rate. Figure 10 shows the water-side overall heat transfer rate as a function of inlet water temperature and flow rate. The figure reveals that the heat transfer rate increases proportionally with the increase of the water temperature. It also shows that the flow rate has a relatively small influence on the heat transfer rate. At 15.6°C (60.0°F), the heat transfer rate improves only 9% when the flow rate increases from 3.2×10^{-4} to 8.2×10^{-4} m^3/s (5.0 to 13.0 gpm). In

ORNL-DWG 82-15432R2

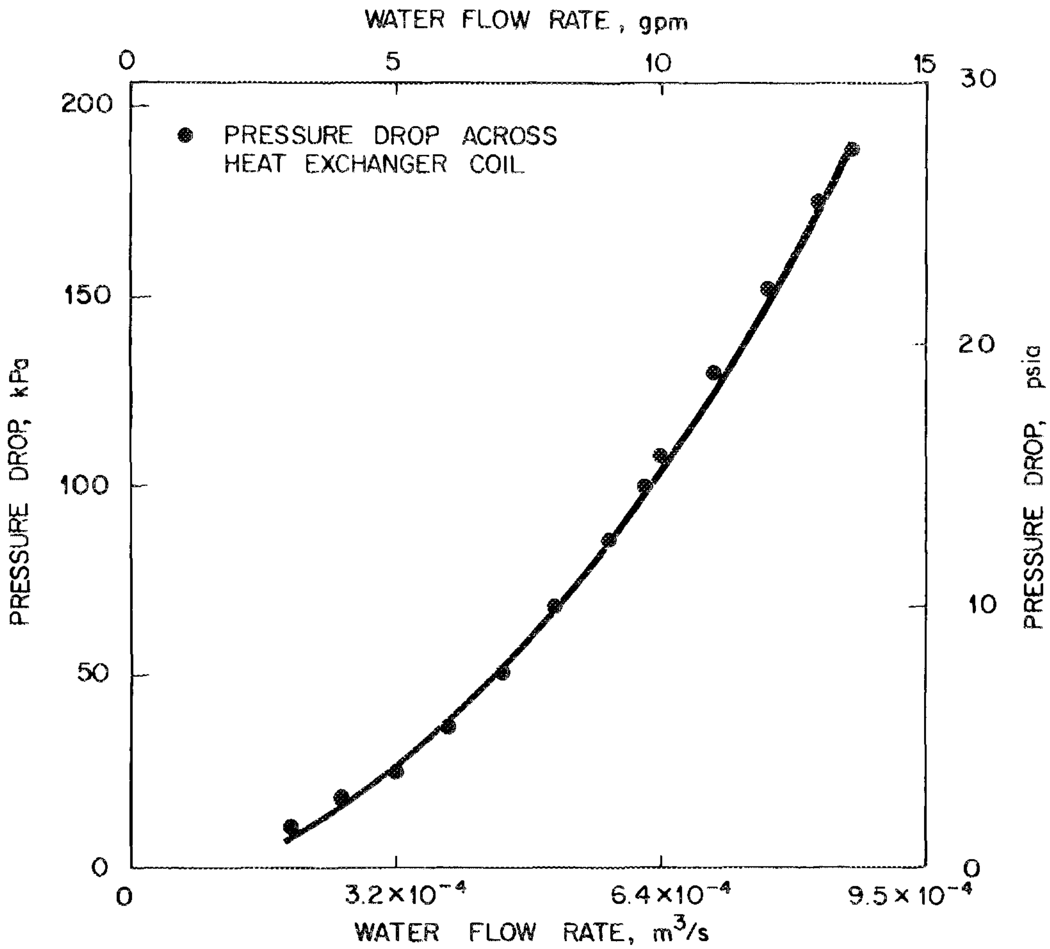

Fig. 9. Effect of water flow rate on water-to-refrigerant heat exchanger pressure drop.

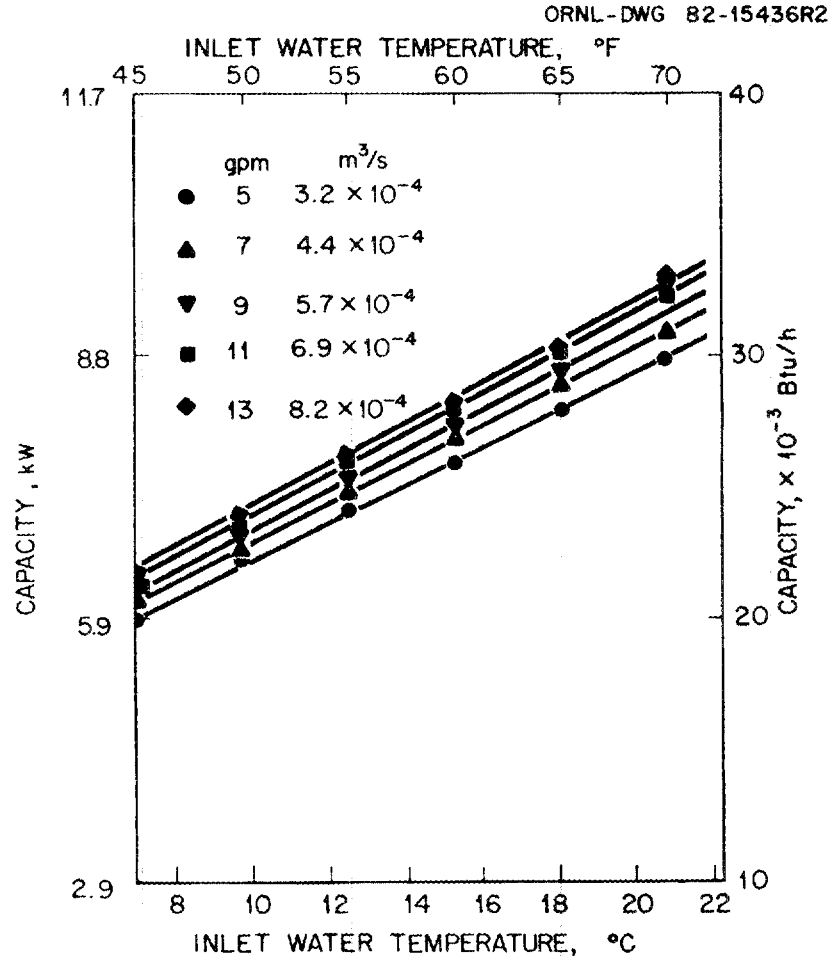

Fig. 10. Water-to-refrigerant heat exchanger heating mode capacity as a function of inlet water temperature and water flow rate.

other words, the heat transfer is more efficient at a lower water flow rate. Figure 11 shows the refrigerant-side pressure drop across the exchanger vs inlet water temperature. It shows that the pressure drop increases with the water temperature and water flow rate because, at higher water temperature and flow rates, the refrigerant flow rate increases.

6.1.4 Fan Performance

The fan was driven by a three-speed motor. The speeds observed in the laboratory were 1130, 1060, and 1020 rpm.

All the tests were performed at a high speed with an external air-side resistance of 39 Pa (0.155 in. water). Figure 12 shows the results of the fan evaluation at high speed; no characteristic curves were obtained for the medium- and low-speed settings. The fan efficiency shown was defined as the ratio of the delivered air power to the electrical power input to the fan motor. It represents the combined efficiency of fan and motor. The efficiency peaked at about 0.43 m^3/s (920.0 cfm) with a value of about 23%. The flow rates used in the heat pump tests ranged from 0.59 to 0.61 m^3/s (1250 to 1300 cfm).

ORNL-DWG 82-15427R2

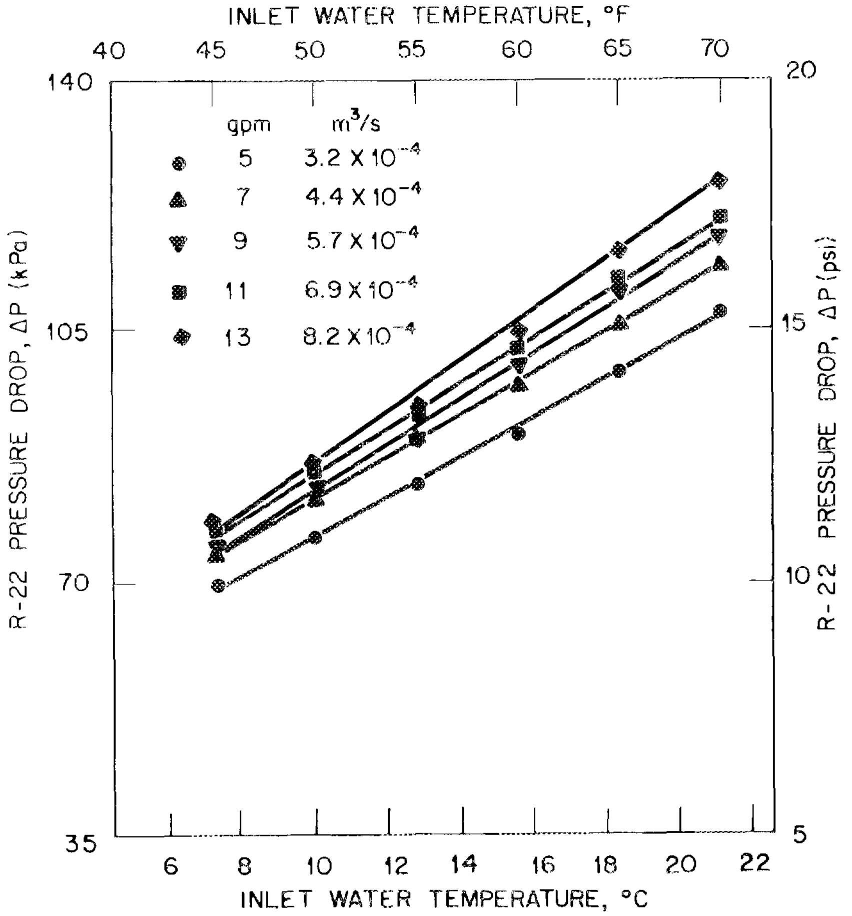

Fig. 11. Refrigerant-side pressure drop of the water-to-refrigerant heat exchanger, in the heating mode.

6.2 Heating Mode Cycling Test Results

Figure 13 shows a typical cycling test at 4.5×10^{-4} m^3/s (7.0 gpm) flow rate and 10.0°C (50.0°F) water temperature. It can be seen that the power input peaked at the start of the cycle. The output increased sharply for the first 60 s and then approached asymptotically toward the steady-state capacity. A great portion of the cycling loss happened during the first minute of operation, when the capacity output was low and power consumption was high.

Figure 14 shows the cycling loss as a function of inlet water temperature with the flow rate as the parameter. Cycling loss is defined as

$$(LOSS)_{cyc} = 1 - \frac{(\mathrm{COP})_{cyc}}{(\mathrm{COP})_{ss}} , \qquad (3)$$

where $(\mathrm{COP})_{cyc}$ is defined as the total capacity output divided by the total power input (no pumping power) for the entire "on" cycle. Figure 14 clearly indicates that the cycling loss is a linear function of inlet water temperature only and is independent of the water flow rate.

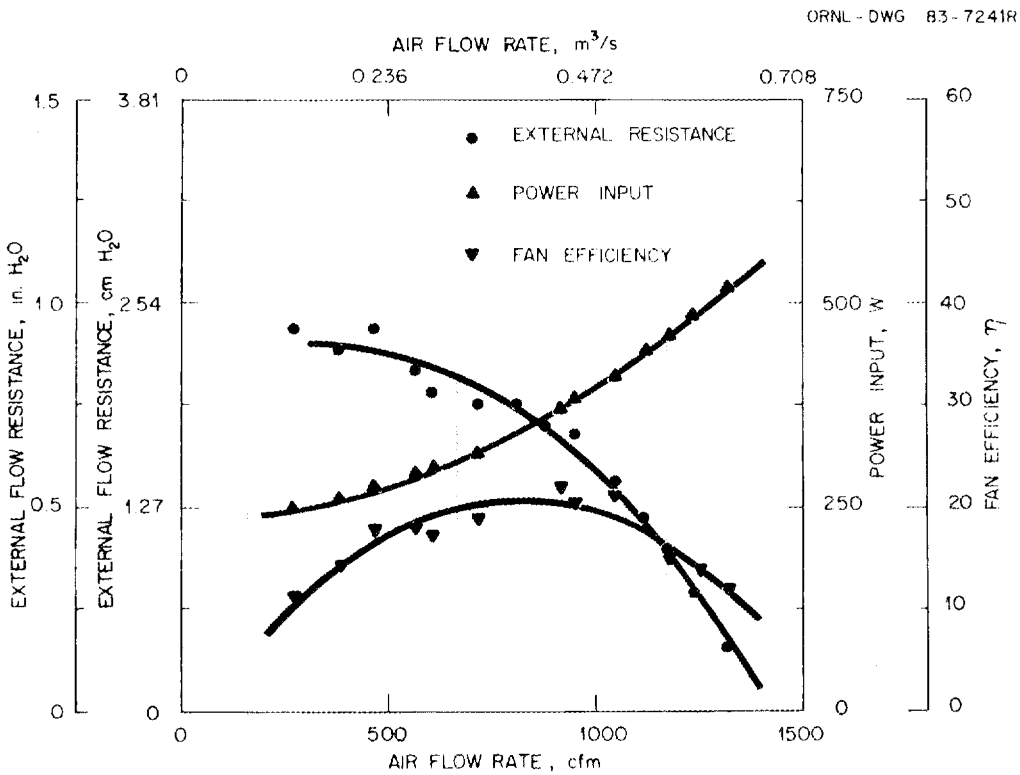

Fig. 12. Fan external pressure, power input, and efficiency as functions of air flow rate.

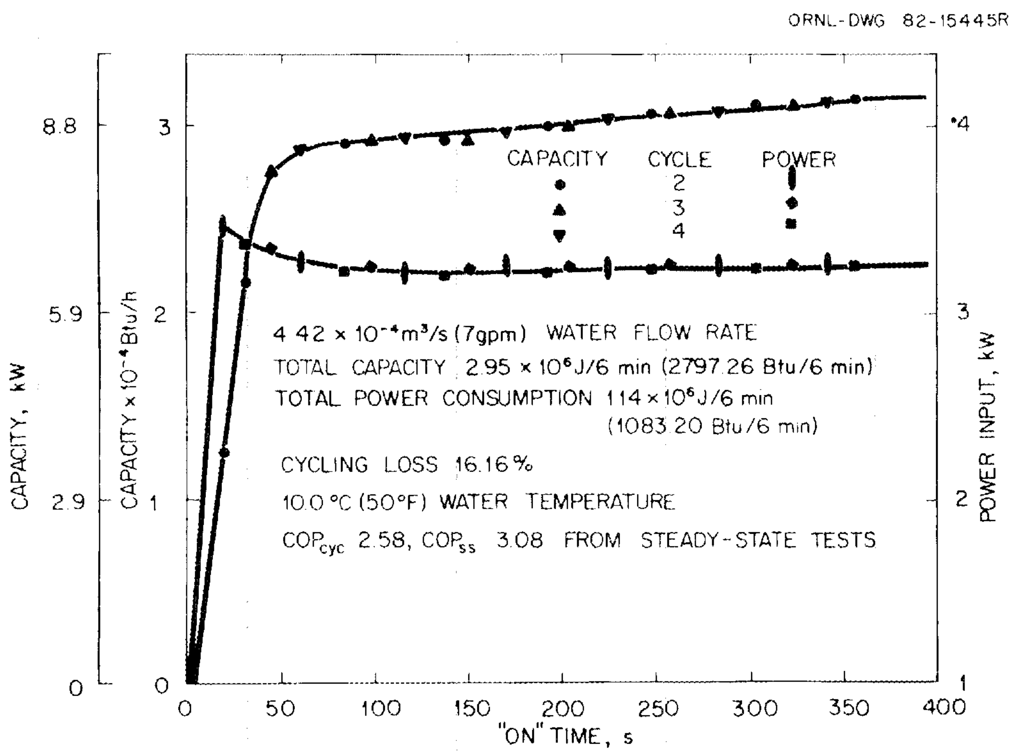

Fig. 13. Heating mode cycling test with output and input as a function of time.

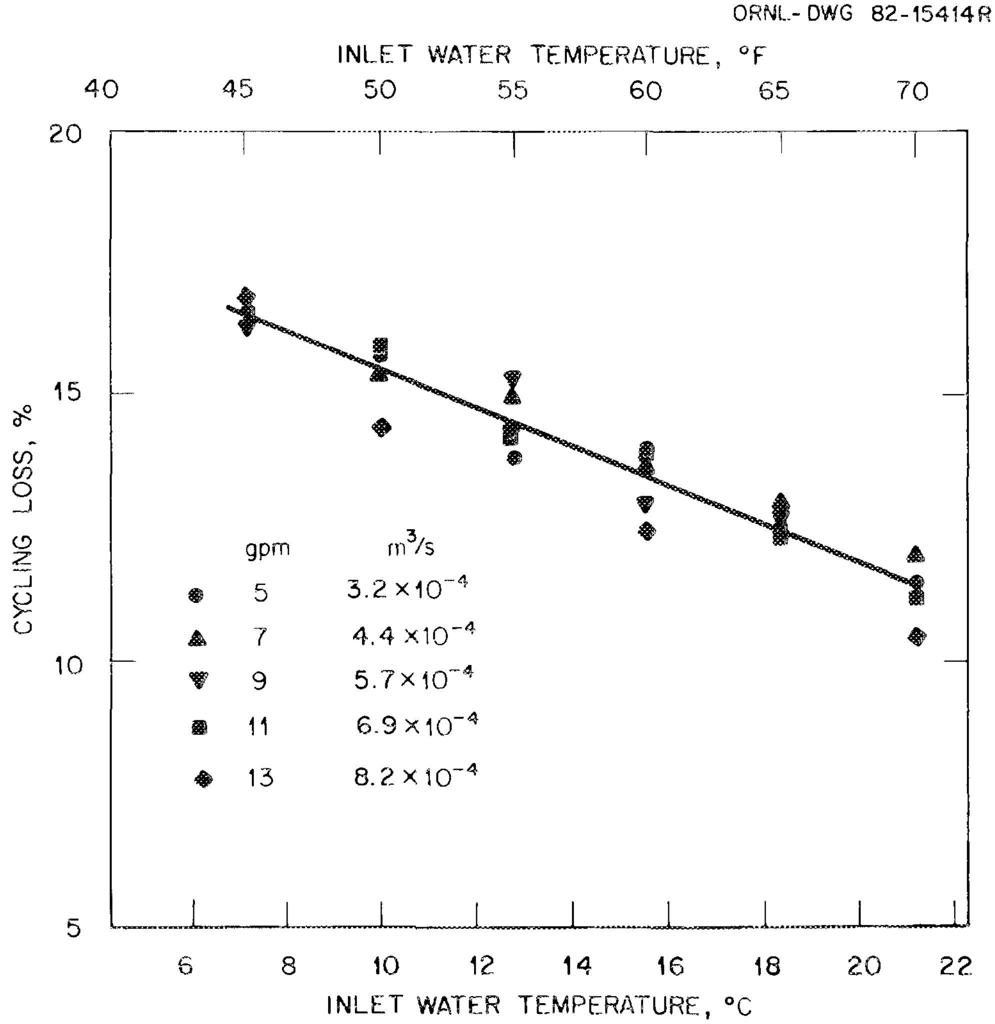

Fig. 14. Heating mode cycling loss as a function of inlet water temperature.

The cycling loss decreases with the increase of water temperature, ranging from 11.3% at 21.1°C (70.0°F) to 16.5% at 7.2°C (45.0°F). The scattering of the test points occurred because the cycling loss was very sensitive to the $(COP)_{cyc}$ and $(COP)_{ss}$. A $\pm 1\%$ deviation of the $(COP)_{ss}$, for example, would mean $\pm 1\%$ change in the cycling loss.

In order to estimate the seasonal performance factor (SPF), the load factor (*LF*) and the degradation coefficient (C_D) were calculated (see Eq. 6, p. 41, for definition of C_D).[1] The load factor is defined as

$$LF = \frac{(\%\ \text{RUN TIME})\ (\text{CAPACITY})_{\text{cyclic}}}{100 \times (\text{CAPACITY})_{\text{steady state}}} . \qquad (4)$$

Figure 15 shows the *LF* as a function of inlet water temperature. It can be seen that the *LF* increases with the increase of water temperature because of the increase of the ratio of the cycle capacity over the steady-state capacity. Figure 16 shows the ratio of the power consumption for the cyclic and steady-state operation, which remained fairly constant at

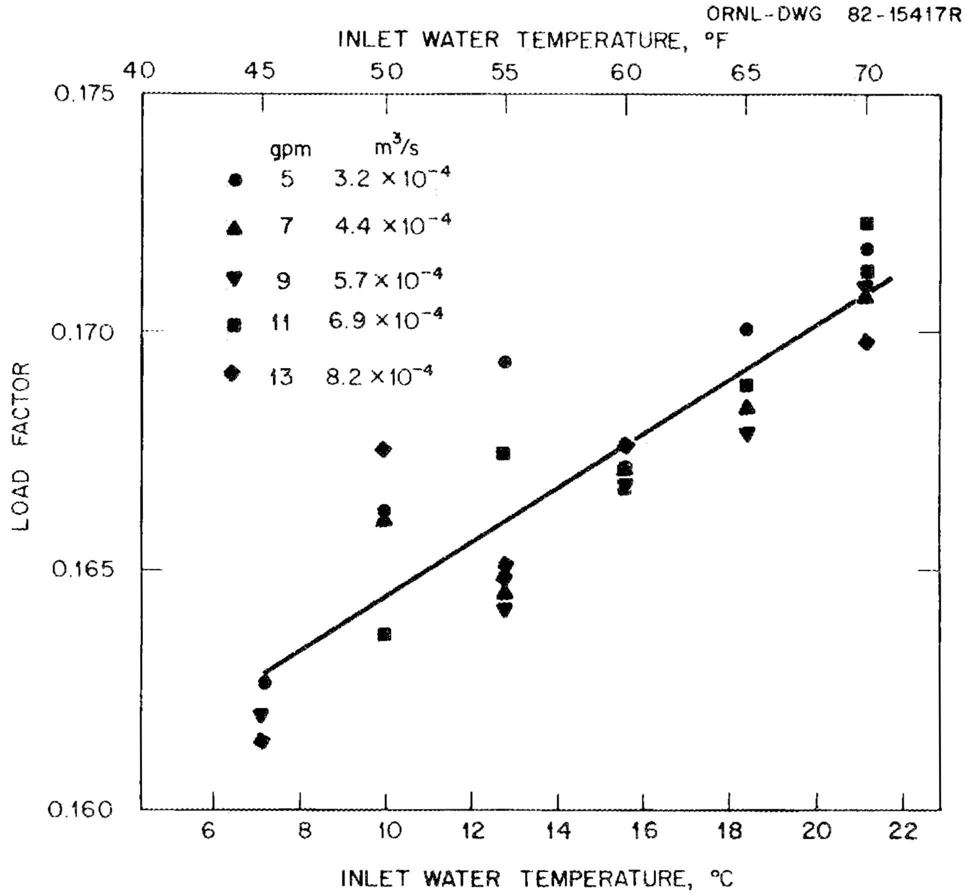

Fig. 15. Heating mode load factor as a function of inlet water temperature.

about 0.97. Figure 17 shows the degradation coefficient, C_D, as a function of inlet water temperature, with water flow rate as the parameter. The results indicate that the degradation coefficient is independent of the water flow rate. The value of C_D varies linearly from 0.2 to 0.14 over the tested water temperature range.

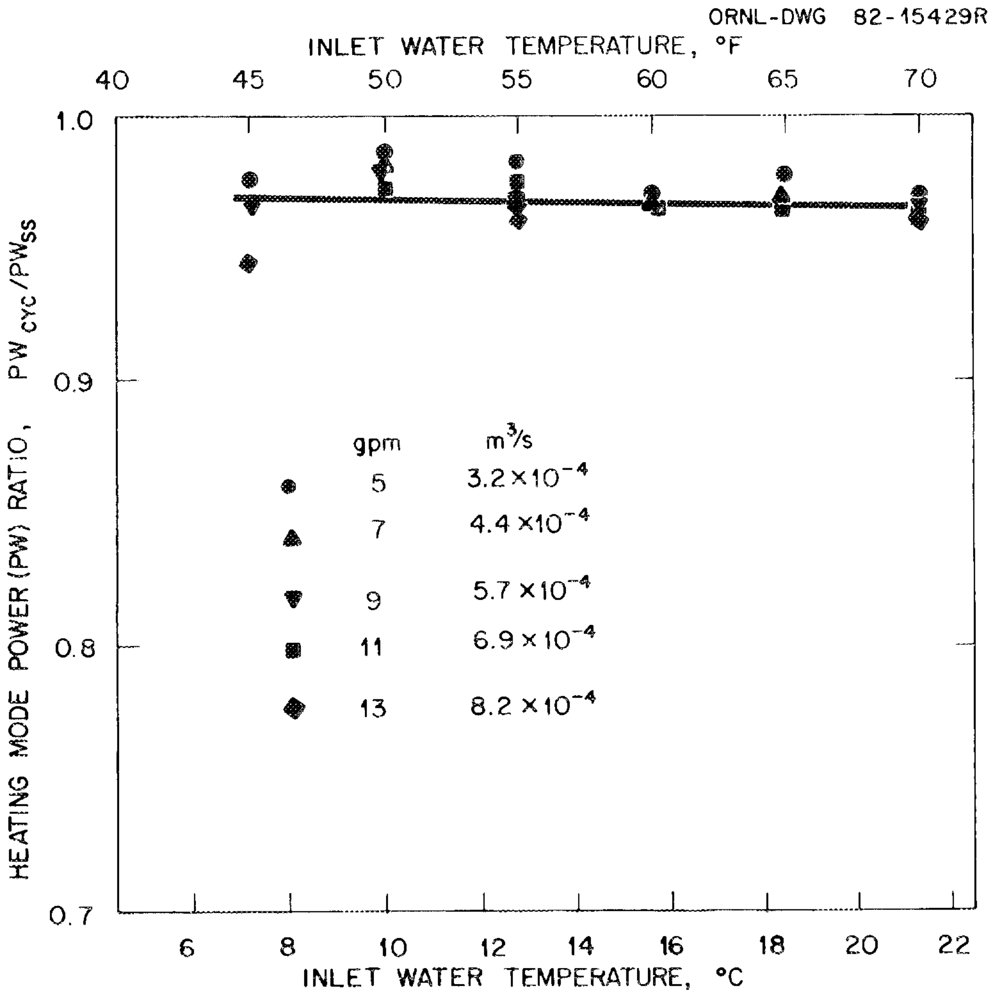

Fig. 16. Heating mode power consumption ratio as a function of inlet water temperature.

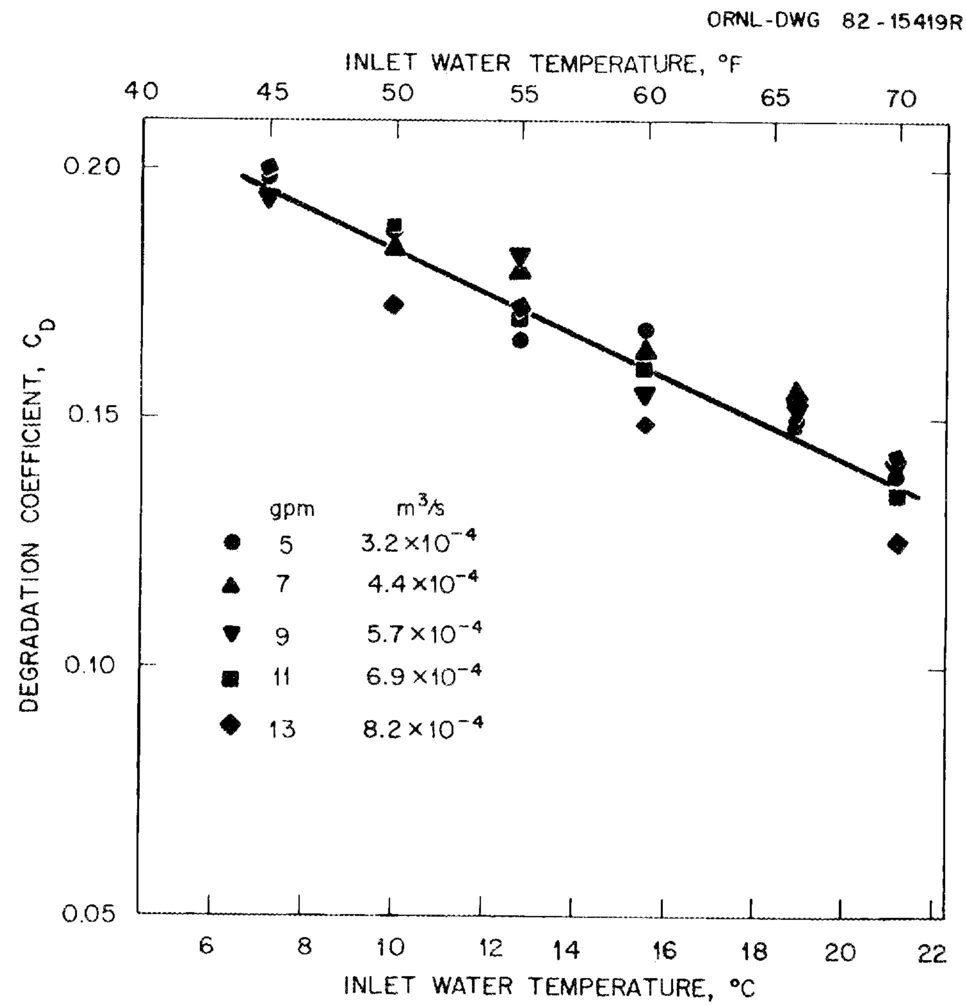

Fig. 17. Heating mode degradation coefficient as a function of inlet water temperature.

7. COOLING MODE STEADY-STATE AND CYCLIC OPERATION TEST RESULTS

7.1 Cooling Mode Steady-State Operation

7.1.1 Effect of Inlet Air Wet-Bulb Temperature

Figures 18, 19, and 20 show the heat pump total and sensible cooling capacities as functions of inlet air wet-bulb temperature at inlet water temperatures of 12.2°C (54.0°F) and 17.2°C (63.0°F) and water flow rates of 3.2×10^{-4} and 5.8×10^{-4} m^3/s (5.0 and 9.0 gpm). The irregular air-side capacity curve in Fig. 19 was caused by the small error in measuring air-side inlet and outlet wet-bulb temperatures. For the same reason, the air-side capacity curve is not shown in Fig. 20. The test results indicate that, as the inlet air wet-bulb temperature is increased, the heat pump total capacity output also increases but the sensible capacity decreases. If we consider the total capacity at 19.4°C (67.0°F) wet bulb as the base point, the ratio of total capacity at specific wet-bulb temperatures to that at 19.4°C (67.0°F) is almost identical for all three tests, even though the tests were performed at different inlet water temperatures and flow rates. The same is also true for sensible capacity, heat rejection, and power output. The average ratios at different wet-bulb temperatures are shown in Table 2. Although the heat pump total and sensible cooling capacities vary considerably with the wet-bulb temperature, the heat rejection varied less than 10% and had almost no effect on the heat pump power input; thus COP also increases with humidity. The data shown in Table 2 enable us to perform the heat pump cooling mode steady-state test at one inlet air wet-bulb temperature and to predict the heat pump performance at different inlet air wet-bulb conditions.

7.1.2 Cooling Capacity and COP

The cooling capacity is defined as the heat absorbed by the coil minus the power input to the indoor fan. The COP is defined as the ratio of cooling capacity to total power input. In this test, the COPs were calculated both with and without the power input to the water pump (Sect. 6.1.1).

Figure 21 shows a typical test result of total capacity output and power input as functions of entering water temperature. It shows that the capacity decreased from 10.7 to 9.5 kW (36,600 to 32,500 Btu/h) and that the power input increased from 2.8 to 3.3 kW, with increasing entering water temperature. Figure 22 shows the total and sensible capacities as functions of entering water temperature with water flow rate as the parameter. The flow rate had little effect on both capacities. At a 12.8°C (55.0°F) entering water temperature, for example, the total capacity increased from 9.7 to 10.2 kW (33,000 to 34,800 Btu/h) as the water flow rate increased from 3.2×10^{-4} to 8.2×10^{-4} m^3/s (5.0 to 13.0 gpm).

Figure 23 shows a typical case of COP as a function of entering water temperature at 5.8×10^{-4} m^3/s (9.0 gpm) water flow rate without including the power input to the pump. The air- and refrigerant-side COPs match very well over the test range of entering water temperature. The COP was correlated as a linear function of entering water temperature. The COP of the refrigerant side varied from 3.8 to 2.9. Figure 24 is the same as

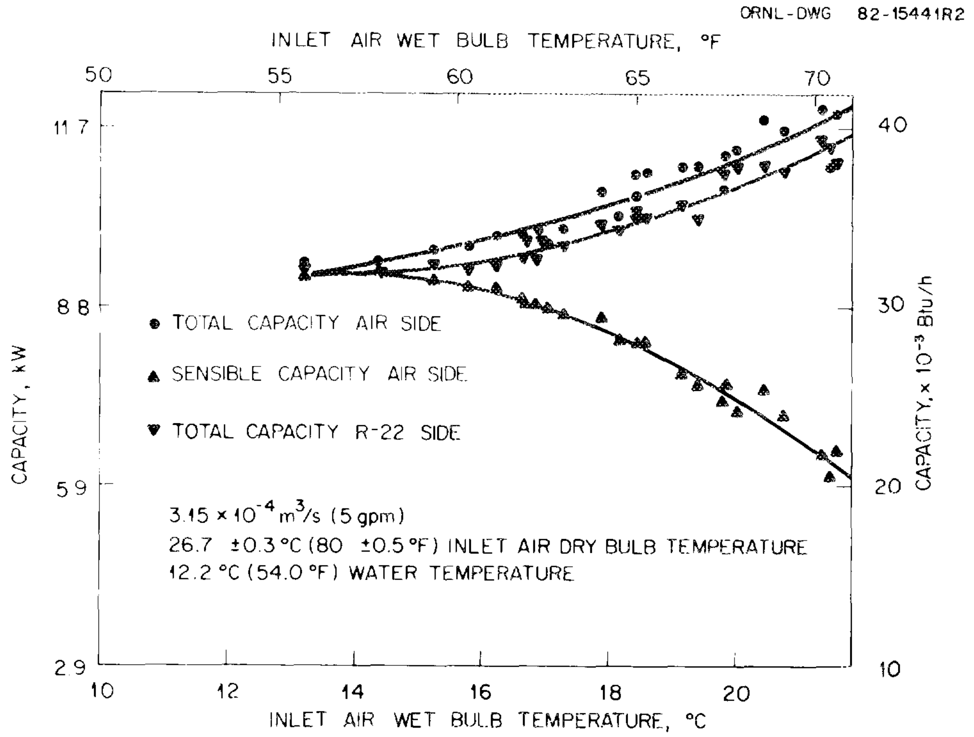

Fig. 18. Effect of inlet air wet-bulb temperature on cooling mode capacity at 3.15 × 10^{-4} m^3/s (5 gpm) water flow rate and 12.2°C (54.0°F) inlet water temperature.

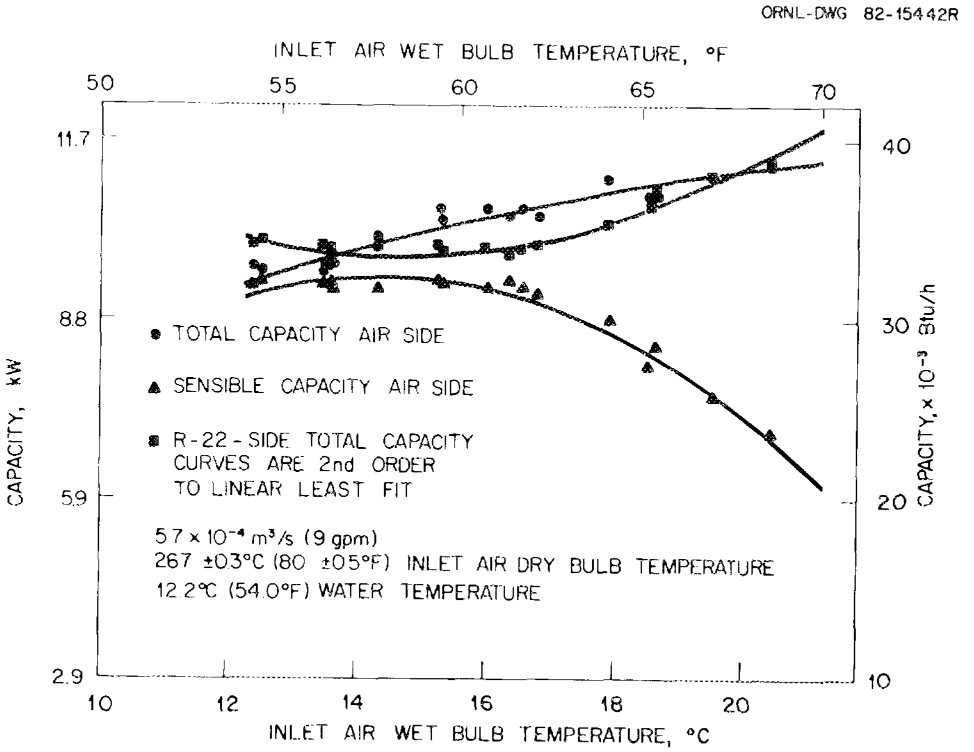

Fig. 19. Effect of inlet air wet-bulb temperature on cooling mode capacities at 5.7 × 10^{-4} m^3/s (9 gpm) water flow rate and 12.2°C (54.0°F) inlet water temperature.

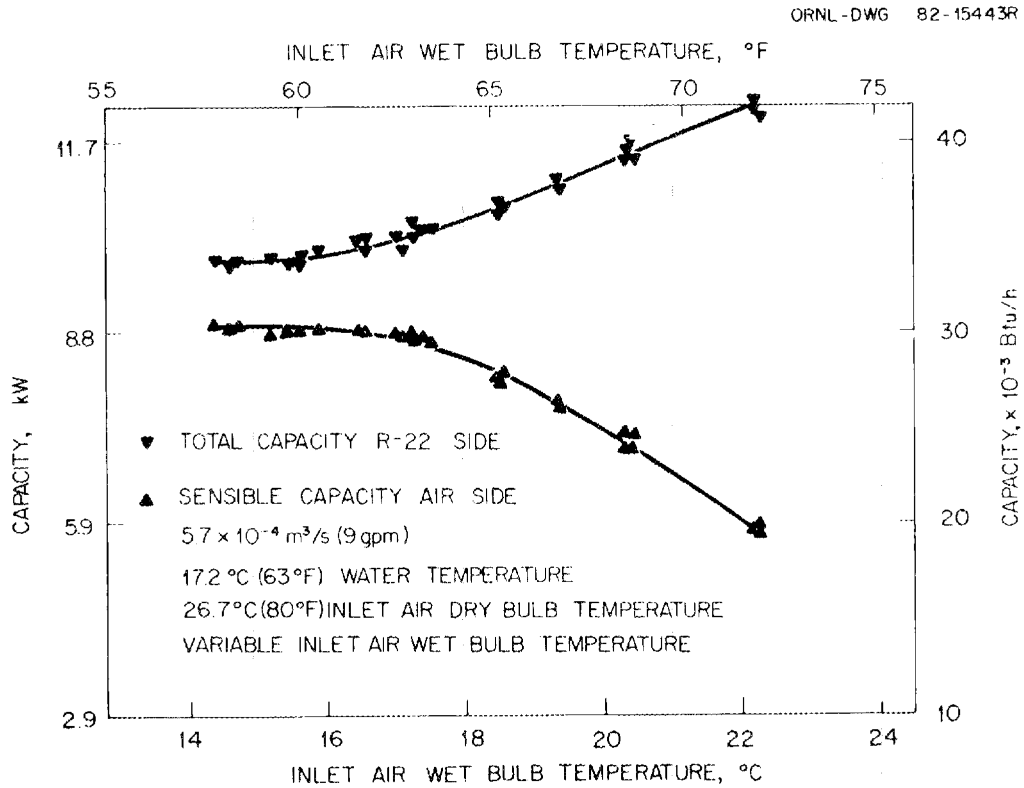

Fig. 20. Effect of inlet air wet-bulb temperature on cooling mode capacities at 5.7×10^{-4} m^3/s (9.0 gpm) water flow rate and 17.2°C (63.0°F) water temperature.

Table 2. Cooling mode performance correction factors for inlet air wet-bulb temperature

Tests performed at 26.7°C (80.0°F) dry-bulb inlet air temperature

Inlet air wet bulb		Sensible capacity	Total capacity	Heat rejected	Power input
°C	(°F)	ratio	ratio[a]	ratio[b]	ratio[c]
21.1	(70.0)	0.852	1.069	1.055	1.009
20.6	(69.0)	0.905	1.045	1.036	1.009
20.0	(68.0)	0.949	1.024	1.019	1.003
19.4	(67.0)	1.00	1.000	1.00	1.00
18.9	(66.0)	1.046	0.979	0.983	0.998
18.3	(65.0)	1.087	0.959	0.968	0.995
17.8	(64.0)	1.123	0.943	0.954	0.993
17.2	(63.0)	1.155	0.927	0.943	0.992
16.7	(62.0)	1.180	0.914	0.933	0.990
16.1	(61.0)	1.201	0.904	0.924	0.989
15.6	(60.0)	1.217	0.895	0.917	0.988
15.0	(59.0)	1.228	0.888	0.912	0.988

[a]Total capacity taken from R-22 side minus the blower power input.
[b]R-22-side heat rejection.
[c]Water pump power consumption not included.

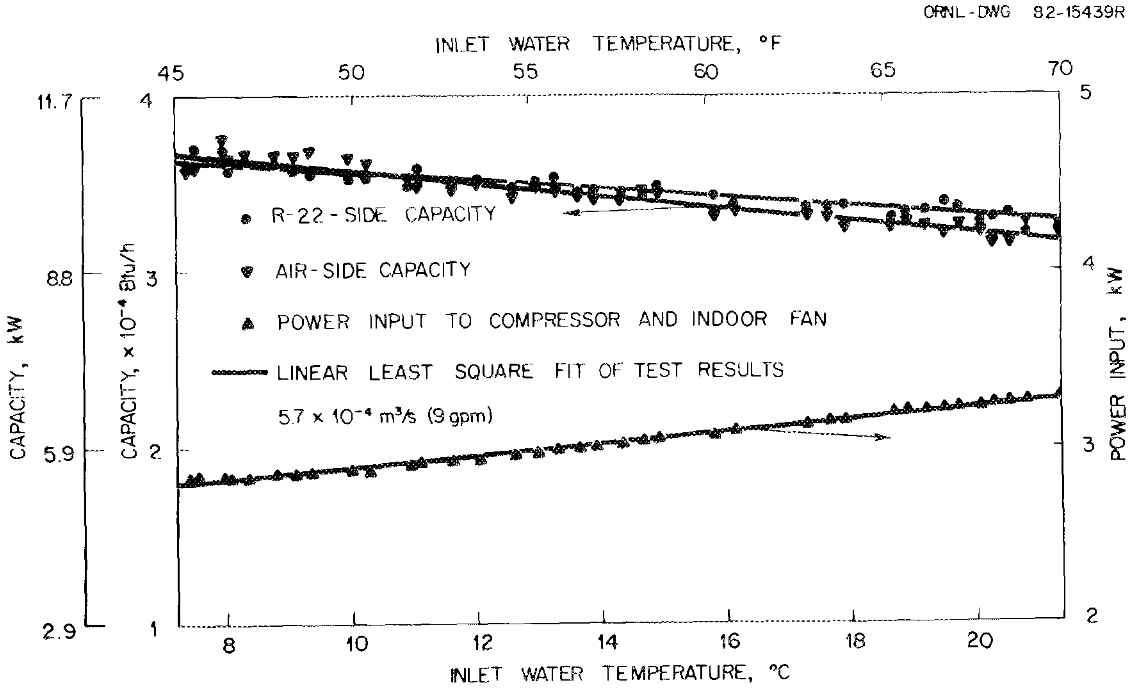

Fig. 21. Cooling mode total capacity as a function of inlet water temperature at 5.7×10^{-4} m^3/s (9.0 gpm) water flow rate.

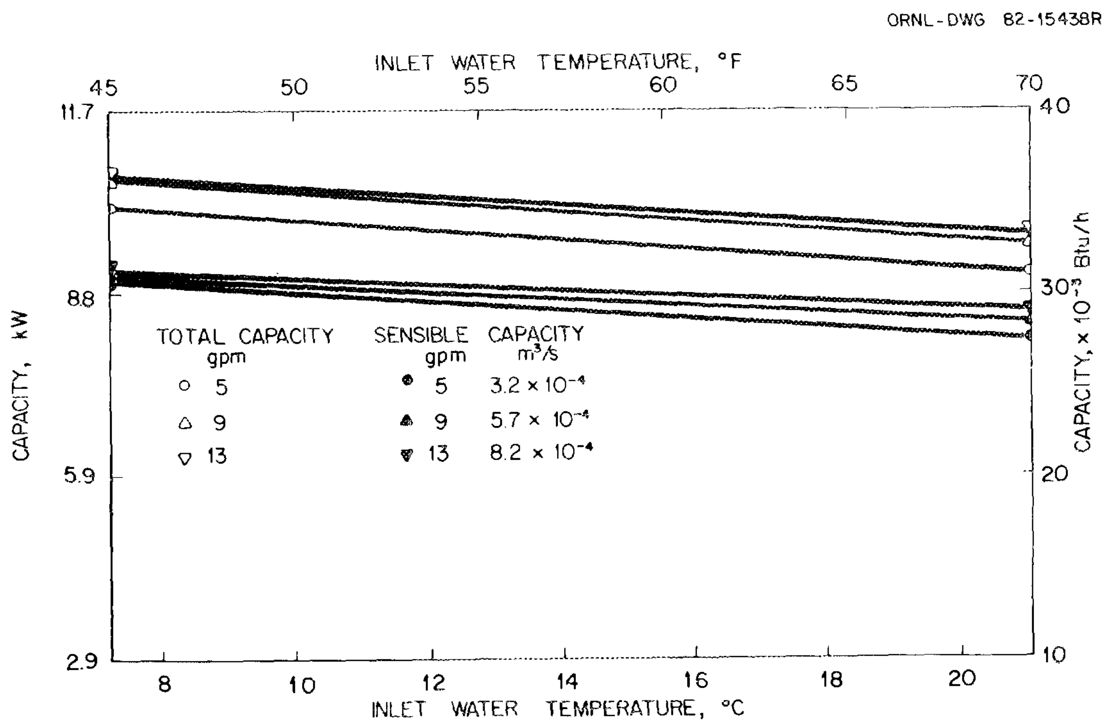

Fig. 22. Cooling mode total and sensible capacities as functions of inlet water temperature and water flow rate.

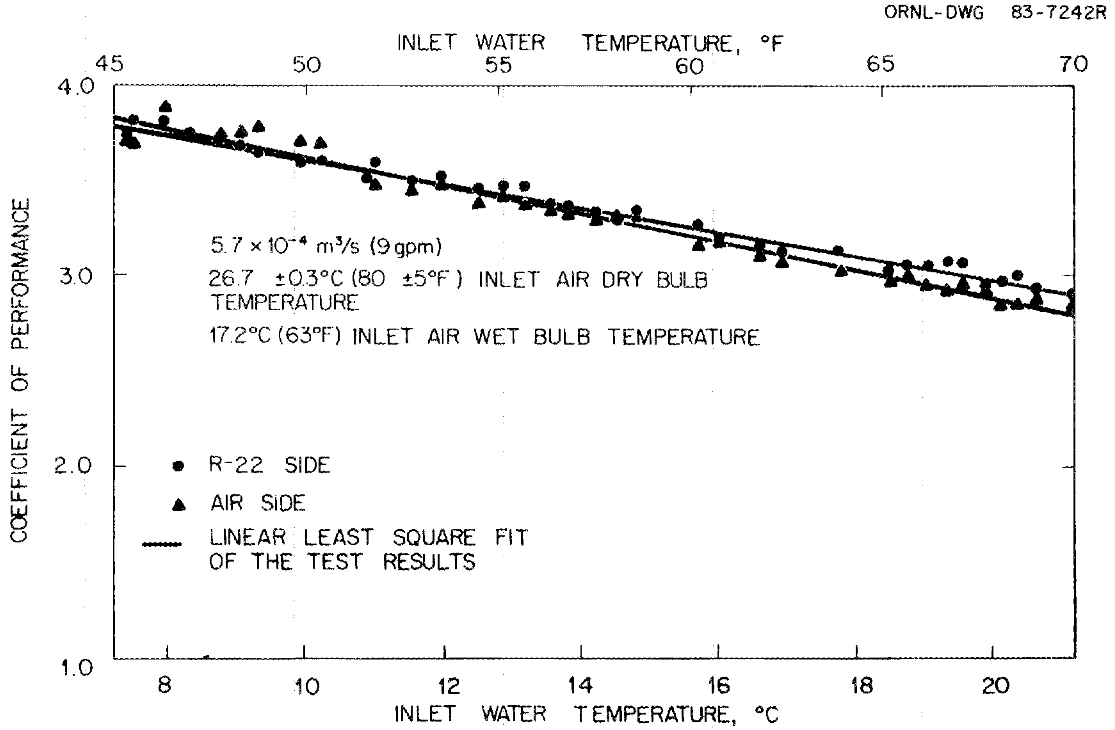

Fig. 23. Cooling mode steady-state COP as a function of inlet water temperature at 5.7 $\times$ 10^{-4} m^3/s (9.0 gpm) water flow rate.

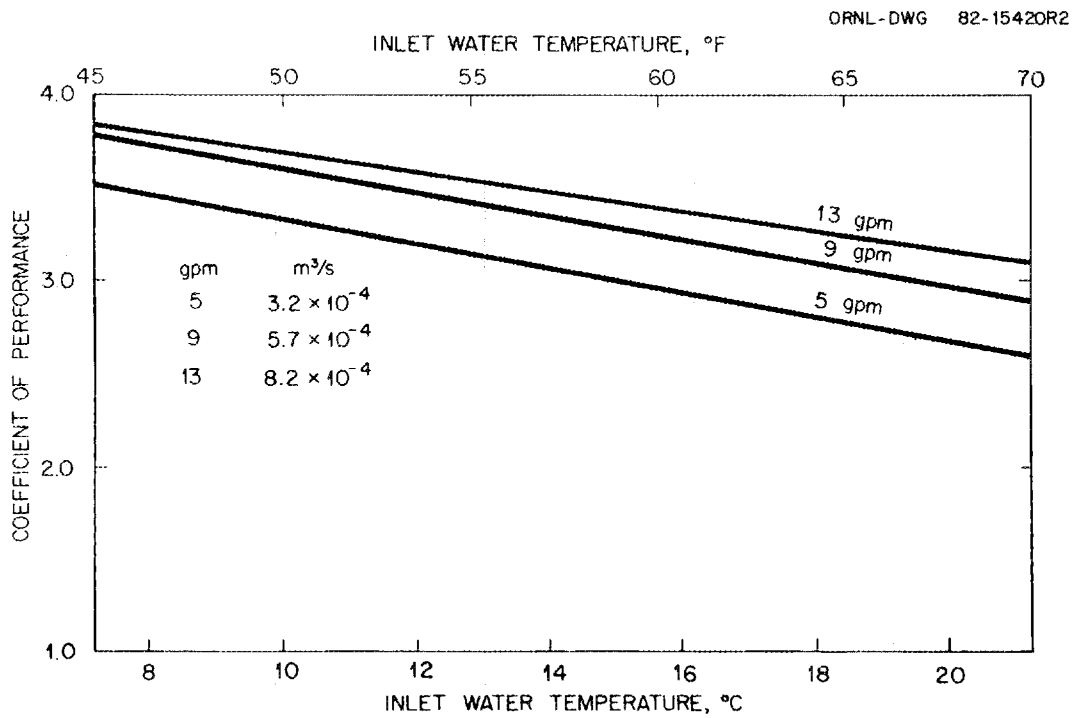

Fig. 24. Cooling mode steady-state COP as a function of inlet water temperature and water flow rate.

Fig. 23, except with water flow rate as the additional parameter. The COP decreases with decreasing water flow rate. At 12.8°C (55.0°F), the COP drops from 3.54 at 8.2×10^{-4} m^3/s (13 gpm) to 3.15 at 3.2×10^{-4} m^3/s (5.0 gpm). Figure 25 is the same as Fig. 24 except that the pump power input for 46 m (150.0 ft) total head (Sect. 4) is included in the COP calculation. With pumping power included, the COP decreases with increasing water flow rate. At 12.8°C (55.0°F), the COP drops from 2.74 to 2.48 when the flow rate is increased from 3.2×10^{-4} to 8.2×10^{-4} m^3/s (5.0 to 13.0 gpm). Once again (as in Sect. 6.1.1), the water pump power input made lower water flow rate operation desirable.

7.1.3 Compressor Operation

The compressor performance parameters are shown in Table 3 at the water flow rate of 5.7×10^{-4} m^3/s (9.0 gpm) and inlet air temperatures of 26.7 ± 0.3°C (80 ± 0.5°F) dry bulb and 17.2 ± 0.3°C (63.0 ± 0.5°F) wet bulb for a range of inlet water temperatures.

The refrigerant flow rate went down with the increase of water temperature because of the decrease in condensing effect by the entering water in the refrigerant water heat exchanger. The pressure ratio increased as the water temperature increased because the discharge pressure was higher when the water temperature was higher. The volumetric efficiency decreased, and yet the combined motor-compressor efficiency increased, with the increase of entering water temperature.

Figure 26 shows the combined motor-compressor efficiency, η_c, and volumetric efficiency, η_v, as functions of inlet water temperature. Unlike heating mode test results, which showed that the efficiencies were independent of water flow rate, the cooling mode volumetric and combined motor-compressor efficiencies depend on the water flow rate, although the effect is very small.

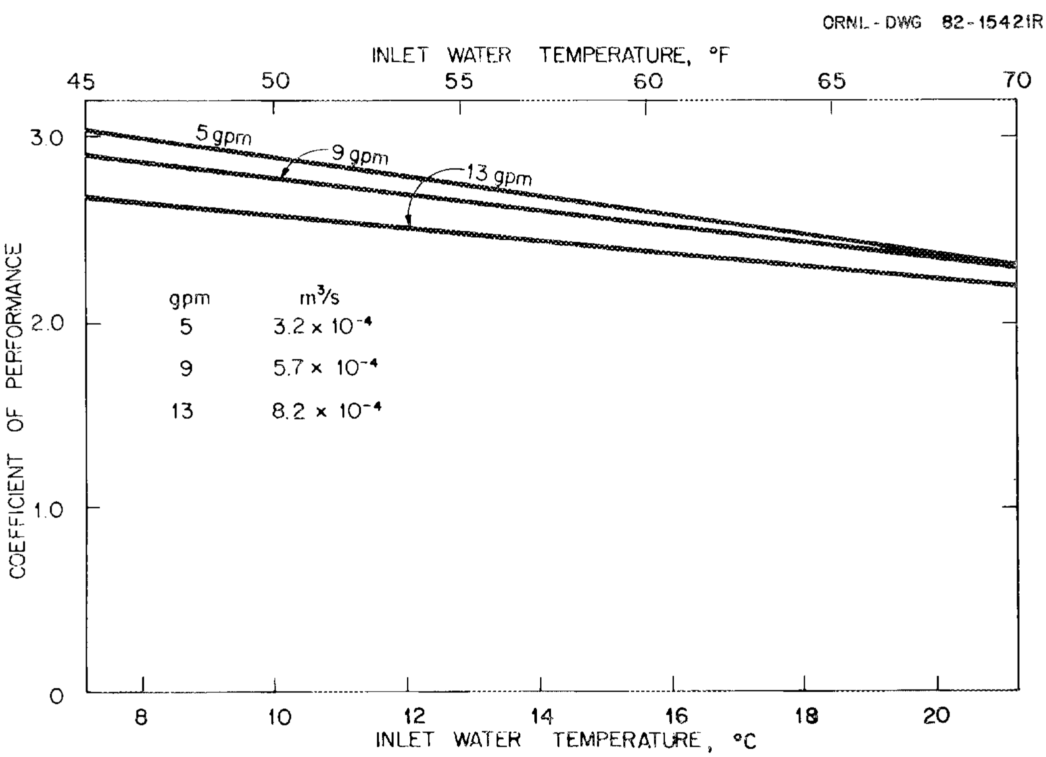

Fig. 25. Cooling mode steady-state COP (with water pumping power) as a function of inlet water temperature and water flow rate.

Table 3. Cooling mode compressor operating characteristics

Heat pump was operated at 5.7 × 10^{-4} m^3/s (9.0 gpm) water flow rate.

Water inlet temperature		Power input to motor	Refrigerant mass flow rate		Pressure ratio	Combined motor-compressor efficiency[a] (η_c)	Volumetric efficiency[a] (η_v)
°C	(°F)	(kW)	kg/h	(lb/h)			
7.2	(45.0)	2.325	208.0	(458.5)	2.00	0.439	0.865
10.0	(50.0)	2.370	206.6	(455.3)	2.06	0.442	0.851
12.8	(55.0)	2.472	208.7	(459.9)	2.10	0.443	0.851
15.6	(60.0)	2.569	207.6	(457.5)	2.34	0.489	0.840
18.3	(65.0)	2.690	202.5	(446.4)	2.49	0.491	0.804
21.1	(70.0)	2.784	203.1	(447.7)	2.68	0.517	0.810

[a]See Table 1 for definitions.

ORNL-DWG 82-15434R

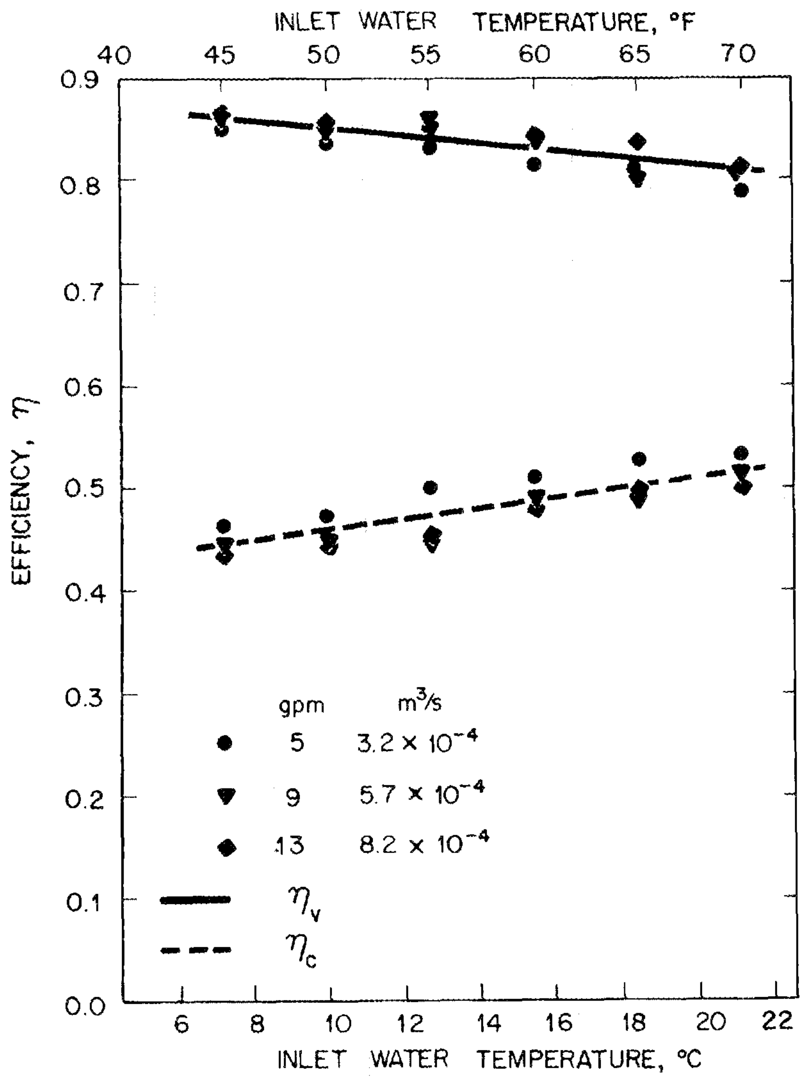

Fig. 26. Cooling mode compressor volumetric (η_v) and combined motor-compressor (η_c) efficiencies as functions of inlet water temperature.

7.1.4 Water-to-Refrigerant Heat Exchanger Performance

The heat exchanger, acting as a condenser for the cooling mode operation, was more complicated to analyze than when used as an evaporator because it has superheated gas, two-phase, and subcooled liquid regions. Only the overall heat transfer rate and discharge pressure as functions of inlet water temperature and water flow rate were analyzed.

The maximum refrigerant pressure across the exchanger was about 55 kPa (8 psi) and was fairly constant.

Figure 27 shows the water-side heat transfer rate as a function of water entering temperature and water flow rate. The overall heat transfer rate was not very sensitive to the water flow rate. One reason was that at low water flow rate, the refrigerant discharge pressure from the compressor went up, which increased the refrigerant discharge temperature, and, as a consequence, the temperature differential between water and refrigerant also increased, which increased the heat transfer between water and refrigerant (Fig. 28).

The above test results suggest that the heat exchanger should be operated at a low water flow rate.

There exists a minimum of the level of liquid refrigerant subcooling at high water flow rates (Fig. 28). This is caused by the change of the refrigerant saturation temperature.

ORNL-DWG 82-15437R

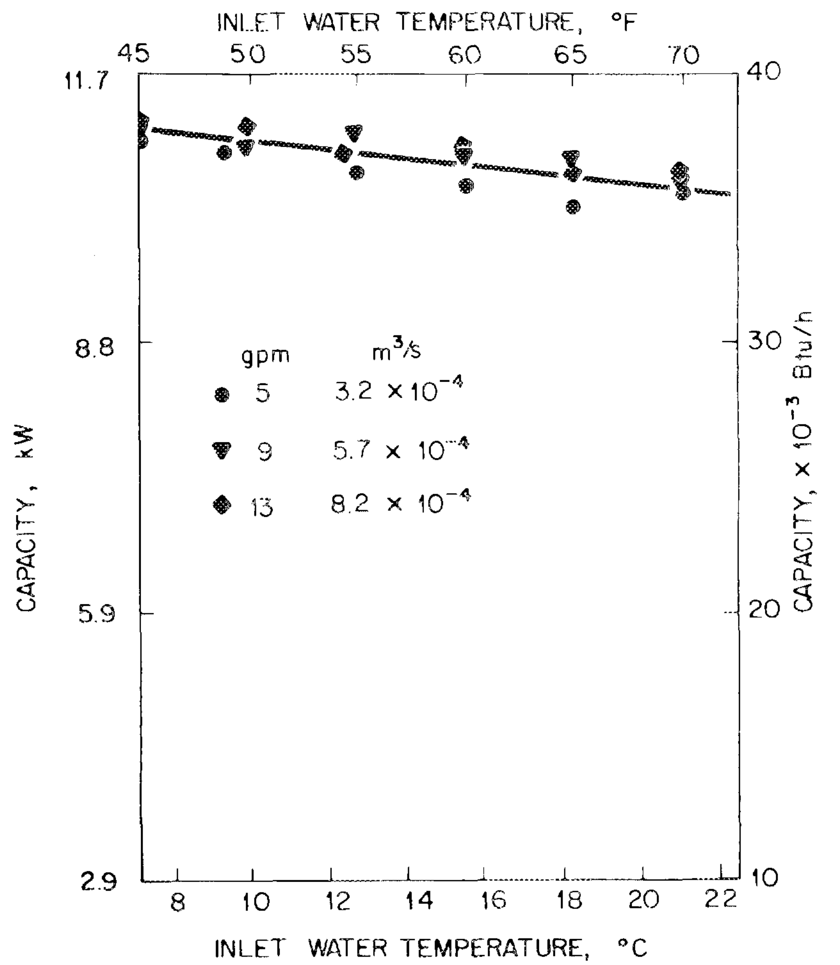

Fig. 27. Cooling mode water-to-refrigerant heat exchanger capacity as a function of inlet water temperature.

ORNL-DWG 82-15428R

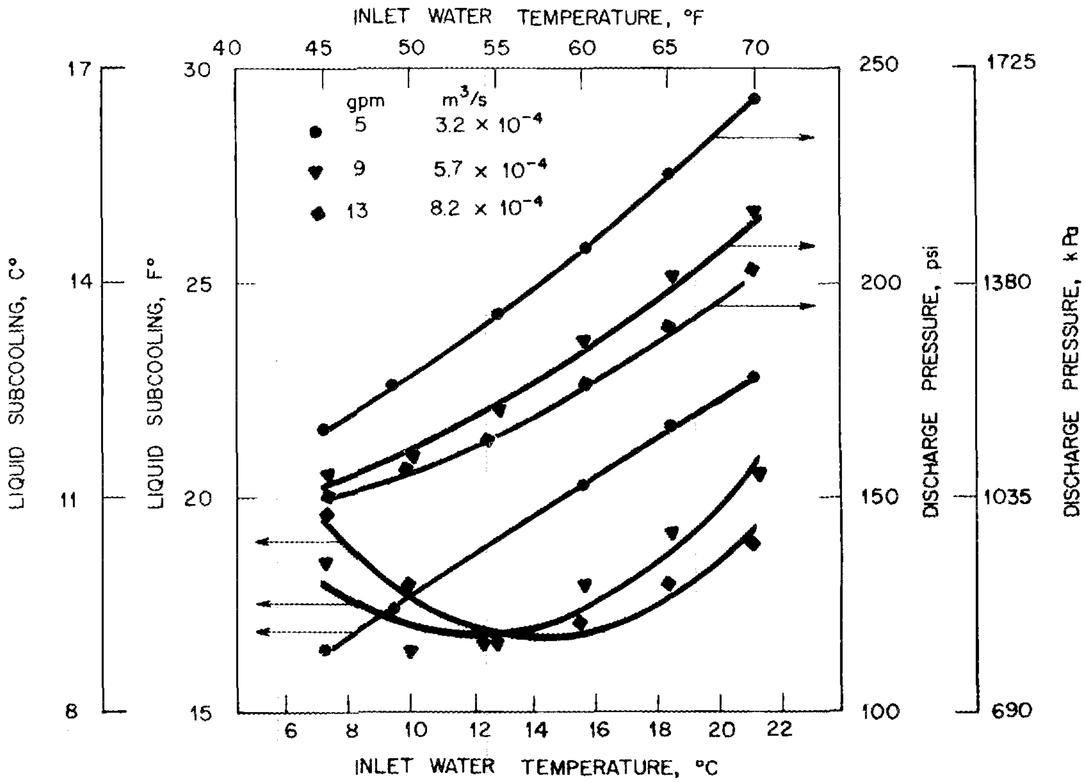

Fig. 28. Cooling mode discharge pressure and condenser exit liquid subcooling as functions of inlet water temperature.

7.2 Cooling Mode Cycling Test Results

7.2.1 Effect of Inlet Air Humidity on Cycling Loss

Figure 29 shows the result of a typical cycling loss test. A great portion of the cycling loss happens during the first 2 min of the "on" cycle when the power input is high and capacity output is low. Figure 30 shows the cycling loss of four tests with inlet air relative humidity as the only variable. Tests results indicate that, below 29% relative humidity, no moisture was condensed. It became a wet coil test when the relative humidity was increased to 37%. Figure 30 confirms Eq. (2); the cycling loss is independent of the inlet air humidity.[6]

7.2.2 Cycling Loss and Degradation Coefficient

Figure 31 shows the cycling loss as a function of inlet water temperature and flow rate. The figure shows that the loss is independent of the water flow rate. The loss increases linearly with the water temperature, ranging from 10.8% at 7.2°C (45.0°F) to 13.5% at 21.1°C (70.0°F).

Figure 32 shows the load factor as a function of water inlet temperature. The load factor decreases with the increase of water temperature, which is due to the decrease of the ratio of cyclic capacity output over the steady-state capacity. Figure 33 shows the degradation coefficient, C_D, as a function of inlet water temperature; C_D increases with water temperature. This value varies from 0.13 to 0.16 over the range of water temperatures tested.

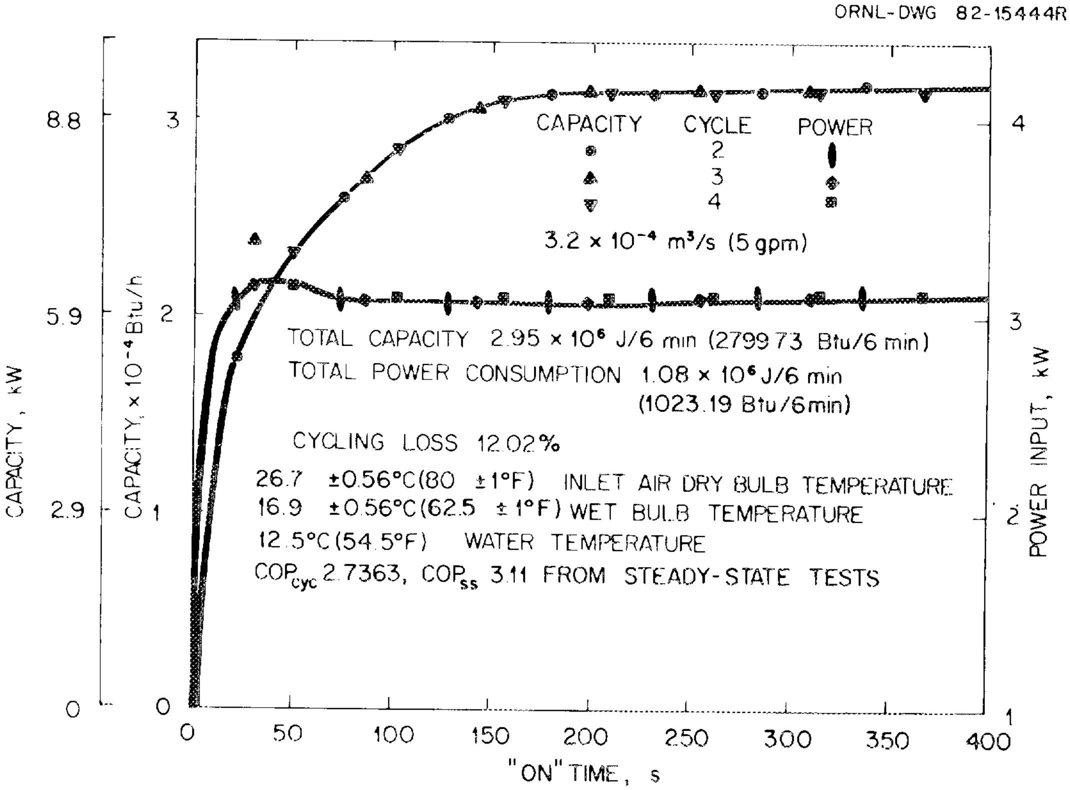

Fig. 29. Cooling mode cycling test with output and input as a function of time at 3.2×10^{-4} m^3/s (5 gpm) water flow rate.

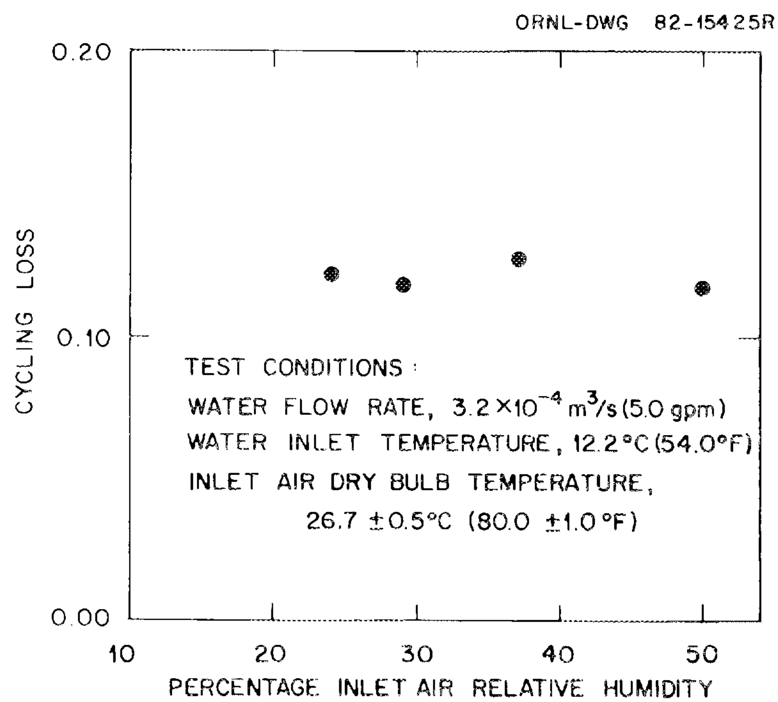

Fig. 30. Effect of inlet air relative humidity on cooling mode cycling loss.

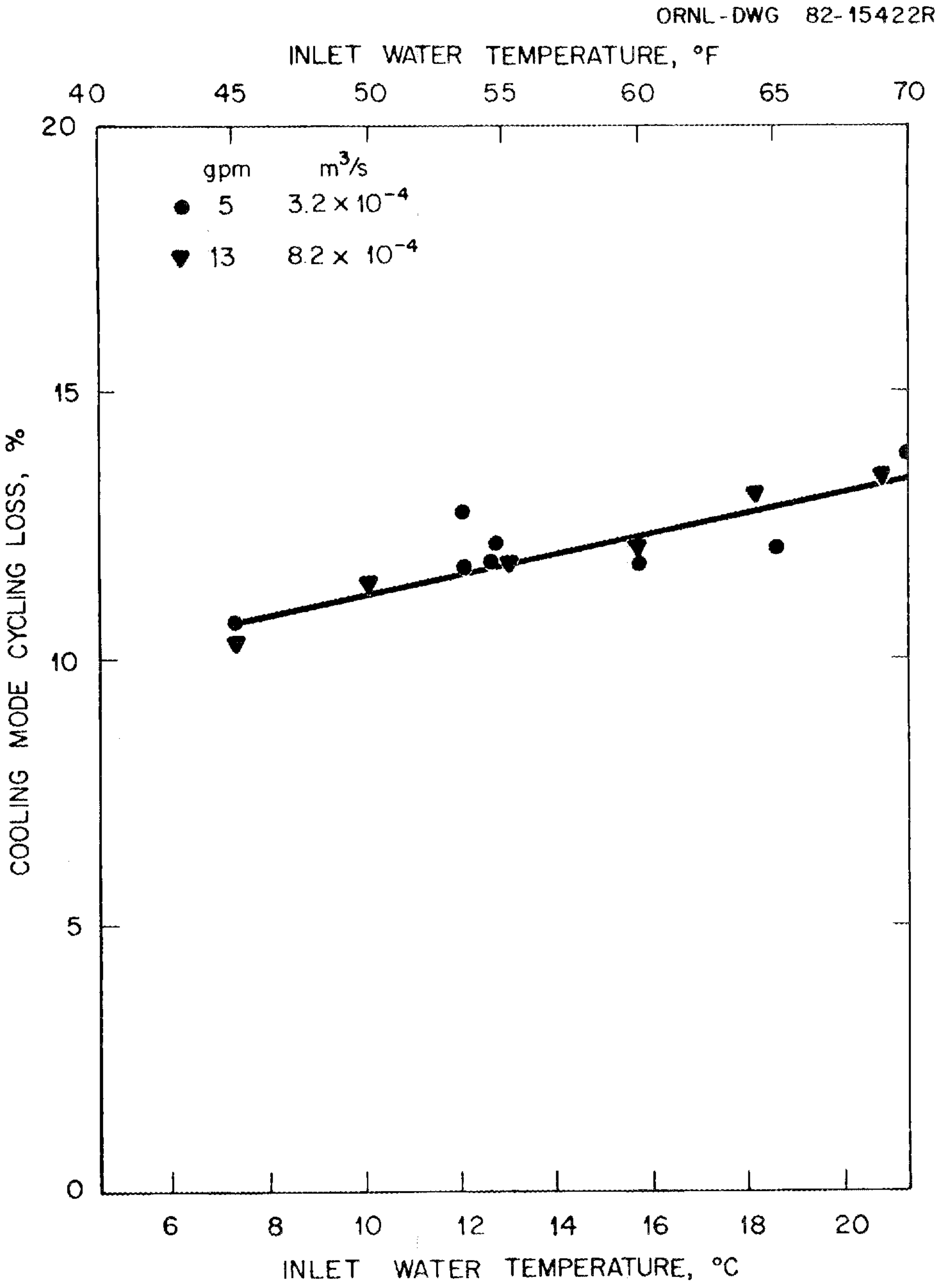

Fig. 31. Cooling mode cycling loss as a function of inlet water temperature.

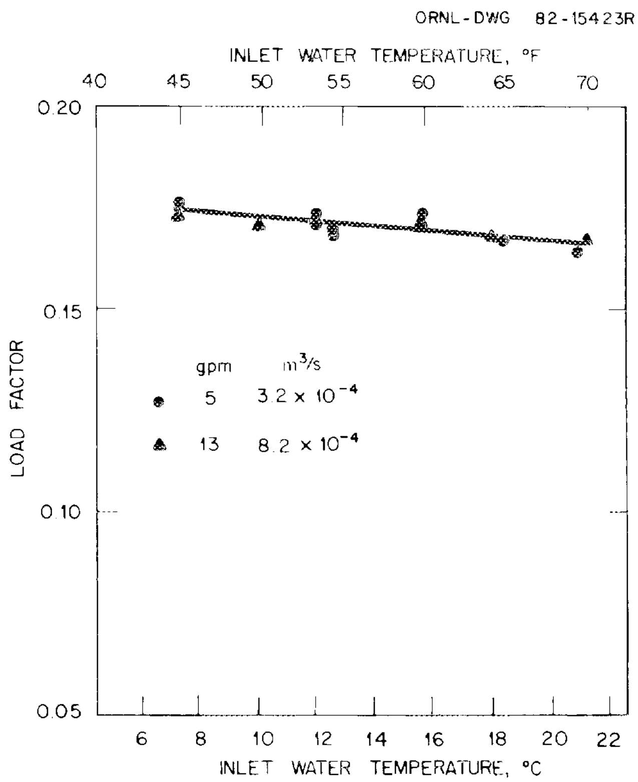

Fig. 32. Cooling mode load factor as a function of inlet water temperature.

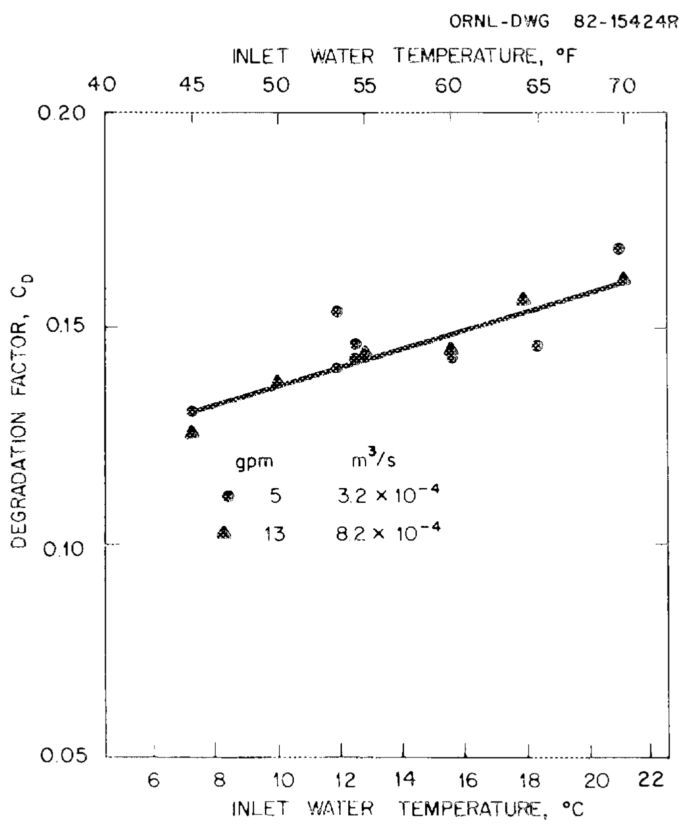

Fig. 33. Cooling mode degradation coefficient as a function of inlet water temperature.

8. A SAMPLE CALCULATION OF WATER SOURCE HEAT PUMP ANNUAL PERFORMANCE FACTORS

The sample calculation is based on an assumed 167-m^2 (1800-ft^2) house located in Nashville, Tennessee, with 12×10^3 kWh (40.9×10^6 Btu) annual heating load and 9.2×10^3 kWh (31.4×10^6 Btu) cooling load respectively. The groundwater temperature is assumed to be 13.9°C (57.0°F). Since the tested heat pump capacity was too high for the house, the capacity and power input were scaled down to 2.5 tons of designed cooling capacity, which was about 10% oversized. To calculate the power input to the water pump, the water head, which includes the depth to water level, the water pressure drop across the water refrigerant heat exchanger, and the frictional loss, was assumed to be 30.5, 45.6, and 61.9 m (100, 150, and 200 ft), along with an assumed pump-motor efficiency of 0.3.

The following steps were taken to calculate the heat pump annual performance factor (APF).

1. The house load, Q_{load}, was calculated by the monthly temperature bin method with the "MAD"[7] computer program.

2. From the heat pump steady-state test results, the steady-state capacity, Q_{ss}, and $(COP)_{ss}$ were found.

3. The load factor was calculated by dividing the house load, Q_{load}, by heat pump steady-state load:

$$LF = \frac{Q_{load}}{Q_{ss}} . \tag{5}$$

4. With the known degradation coefficient, C_D, the $(COP)_{cyc}$ was calculated with the following equation:

$$C_D = \frac{1 - [(COP)_{cyc}/(COP)_{ss}]}{1 - LF} . \tag{6}$$

5. The power input to the heat pump was estimated by dividing Q_{load} by $(COP)_{cyc}$.

6. The heat pump APFs were calculated by summing the house load, both heating and cooling, and then dividing it by the total power input into the system, which included the power input to the compressor motor, fan motor, and water pump motor.

The degradation coefficient, C_D, used was 0.168 for the heating mode and 0.147 for the cooling mode as determined by the test for a source water temperature of 13.9°C (55.0°F).

Table 4 shows the heat pump heating and cooling capacities and COP as functions of water flow rate but without water pumping power. Capacity and COP scaling-down factors used are also shown in the table. Table 5 shows the water pump power consumption as a function of water flow rate and pump head. Table 6 shows the APF as a function of water flow rate per ton of cooling and total pump head with cycling loss. The data listed in Table 6 are shown graphically in Fig. 34. It is clear that the APF is strongly affected by the total head.

Table 4. Steady-state water source heat pump performance data

Heat pump entering water temperature was 13.9°C (57.0°F).
C_D (degradation coefficient) = 0.168 for heating and 0.147 for cooling

Water flow rate		Heating mode			Cooling mode			8.79-kW (2.5-ton) scaling factor
		Capacity		COP[a]	Capacity		EER[a]	
m^3/s	(gpm)	kW	(Btu/h)		kW	(Btu/h)		
1.9×10^{-4}[b]	(3.0)	10.2	(34,700)	3.12	8.9	(30,500)	9.39	0.987
3.2×10^{-4}	(5.0)	10.5	(35,900)	3.15	9.5	(32,500)	10.51	0.926
5.8×10^{-4}	(9.0)	11.1	(37,800)	3.22	10.1	(34,500)	11.47	0.872
8.2×10^{-4}	(13.0)	11.5	(39,200)	3.30	10.2	(34,700)	11.88	0.867

[a]COP and energy efficiency ratio (EER) were calculated without including water pump power input.
[b]The data on this water flow rate were extrapolated.

Table 5. Assumed water pump power input

Pump power input calculation was under the assumption of pump efficiency equal to 0.3 (see Sect. 4 for detailed pump power input calculation).

Water flow rate		Water pump power input (W)		
m^3/s	(gpm)			
1.9×10^{-4}	(3.0)	188[a]	282[b]	376[c]
3.2×10^{-4}	(5.0)	314	471	628
5.8×10^{-4}	(9.0)	565	848	1130
8.2×10^{-4}	(13.0)	817	1225	1634

[a]Values in this column are for an assumed total head of 30.5 m (100 ft).
[b]Values in this column are for an assumed total head of 45.7 m (150 ft).
[c]Values in this column are for an assumed total head of 61 m (200 ft).

Table 6. Water source heat pump annual performance factor

With cycling loss

Water flow rate/unit cooling capacity		Annual performance factor			C_D	
$m^3/s \cdot kW$	(gpm/ton)				Heating	Cooling
0.21×10^{-4}	(1.18)	2.54[a]	2.47[b]	2.40[c]	0.168	0.147
0.34×10^{-4}	(1.85)	2.59	2.46	2.37		
0.57×10^{-4}	(3.13)	2.54	2.36	2.21		
0.85×10^{-4}	(4.50)	2.44	2.22	2.03		

[a]Total pump head values for this column: 30.5 m (100.0 ft).
[b]Total pump head values for this column: 45.7 m (150.0 ft).
[c]Total pump head values for this column: 61.0 m (200.0 ft).

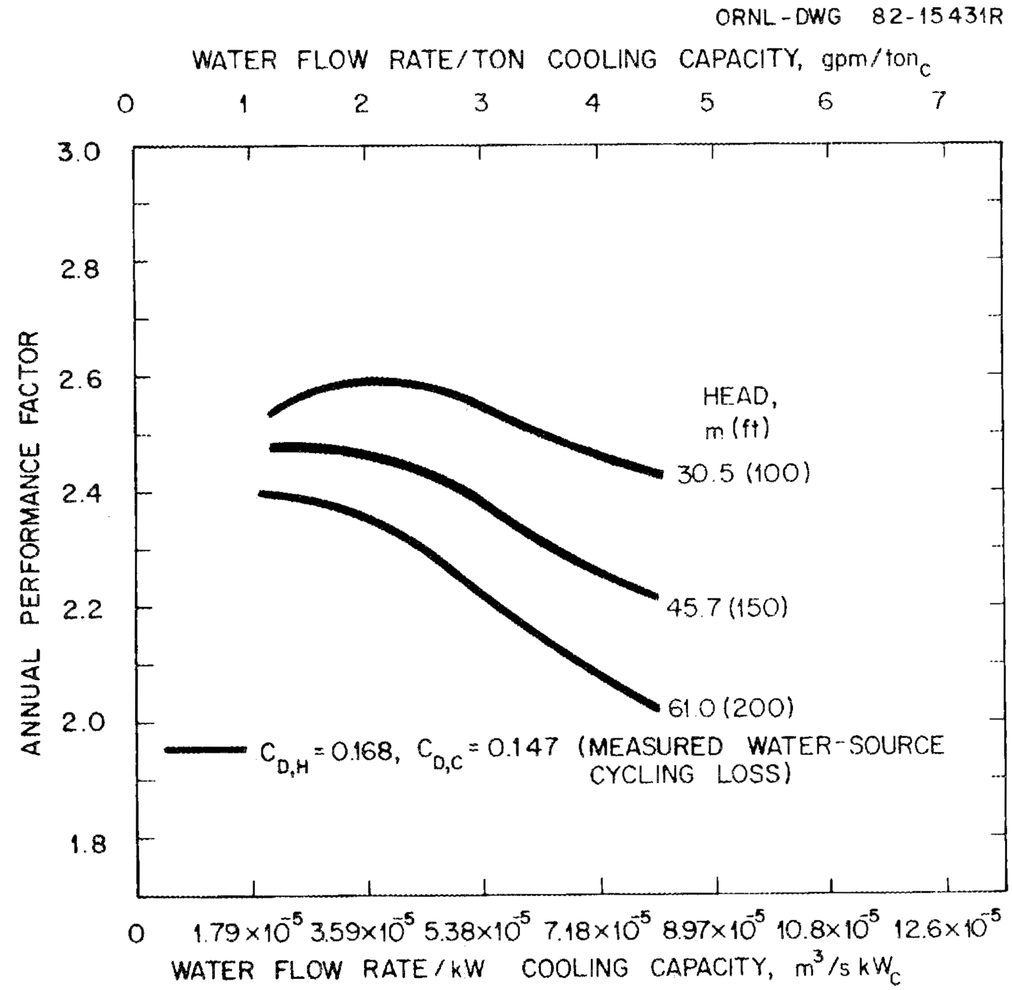

Fig. 34. Annual performance factor as a function of water flow rate per unit of cooling capacity and total head.

REFERENCES

1. D. A. Didion and G. E. Kelly, "New Testing and Rating Procedures for Seasonal Performance of Heat Pump," *ASHRAE J.*, pp. 40-44 (September 1979).
2. *Thermocouple Conversion Tables,* National Bureau of Standards Circular 561.
3. A. A. Domingorena and S. J. Ball, *Performance Evaluation of a Selected Three-Ton Air to Air Heat Pump in the Heating Mode,* ORNL/CON-34, Oak Ridge National Laboratory, January 1980.
4. *Thermodynamic Properties of Freon 22,* DuPont, Technical Literature, T-22, 1964.
5. *ASHRAE Handbook: 1981 Fundamentals,* Chap. 5, American Society of Heating, Refrigerating and Air-Conditioning Engineers, Inc., Atlanta, 1981.
6. W. Parken, Jr., R. W. Beausolid, and G. E. Kelly, "Factors Affecting the Performance of a Residential Air to Air Heat Pump," *ASHRAE Trans.* 83, Part I (1977).
7. M. L. Ballou, E. A. Nephew, and L. A. Abbatiello, *MAD: A Computer Program for ACES Design Using Monthly Thermal Loads,* ORNL/CON-51, Oak Ridge National Laboratory, March 1981.

INTERNAL DISTRIBUTION

1. S. J. Ball
2. V. D. Baxter
3. J. L. Bledsoe
4. R. S. Carlsmith
5. F. C. Chen
6. N. C. J. Chen
7. J. E. Christian
8. N. Domingo
9. D. M. Eissenberg
10. P. D. Fairchild
11. S. K. Fischer
12. W. Fulkerson
13. V. O. Haynes
14. K. E. Heidenreich
15. N. E. Hinkle
16. B. Honea
17. W. R. Huntley
18. W. L. Jackson
19. L. Jung
20. F. R. Kalhammer, Consultant
21. S. I. Kaplan
22. S. V. Kaye, Consultant
23. T. R. LaPorte, Consultant
24. W. P. Levins
25. T. S. Lundy
26. L. McCold
27. H. A. McLain
28. V. C. Mei
29. J. W. Michel
30. W. A. Miller
31. R. E. Minturn
32. W. R. Mixon
33. L. I. Moss, Consultant
34. J. C. Moyers
35. M. Olszewski
36. H. Perez-Blanco
37. C. H. Petrich
38. C. K. Rice
39. M. W. Rosenthal
40. C. Snyder
41. C. A. Srite
42. T. Stovall
43. W. H. Williams, Consultant
44. Biology Division Library

45–46. Central Research Library

47. Document Reference Section
48. Laboratory Records (RC)

49–50. Laboratory Records Department

51. ORNL Patent Section

EXTERNAL DISTRIBUTION

52. Phil Albertson, Manager, Charles Machine Works, Inc., P.O. Box 66, Perry, OK 73077
53. C. H. Atkinson, Environmental Division, Acres Consulting Serv., Ltd., 5259 Dorchester Road, Niagara Falls, Ontario 12E G61
54. B. Backstrom, Chalmers University of Technology, Jordvarme Gruppen, S-41296, Goteborg, Sweden
55. Michael K. Bergman, Staff Scientist, American Public Power Assoc., 2301 M Street, N.W., Washington, DC 20037
56. Prof. Jacob Bigeleisen, Department of Chemistry, State University of New York at Stoneybrook, Stoneybrook, NY 11794
57. W. Z. Black, Professor, School of Mech. Eng., Georgia Institute of Technology, Atlanta, GA 30332
58. James E. Bose, School of Technology, Oklahoma State University, Stillwater, OK 74078
59. R. A. Budenholzer, Department of MMAE, Ill. Institute of Technology, 3110 S. State Street, Chicago, IL 60616
60. David Cabot, President, Avondale Solar Corporation, P.O. Box 501, 44 Avondale Road, Westerly, RI 02891

61–65. James M. Calm, Project Manager, Heat Pump Development, Electric Power Res. Inst., 3412 Hillview Avenue, Palo Alto, CA 94303

66. Lee Culpepper, TVA, 330 401 Building, Chattanooga, TN 37401
67. Barry J. Dempsey, Dept. of Civil Engineering, University of Illinois, Urbana, IL 61801
68. R. J. Denny, Air-Conditioning & Refrigeration Institute, 1815 N. Fort Meyer Drive, Arlington, VA 22209
69. Charles E. Dorgan, University of Wisconsin, 825 Extension Building, 432 North Lake Street, Madison, WI 53706
70. Richard Dougall, Dept. of Mechanical Engineering, University of Pittsburgh, Pittsburg, PA 15261
71. G. D. Duffy, Air Conditioning News, P.O. Box 2600, Troy, MI 48007
72. David G. Dutton, Vice President—Marketing, McElroy Manufacturing, Inc., P.O. Box 15580, Tulsa, OK 74112
73. John A. Edwards, North Carolina State University, Department of Mechanical and Aerospace Engineering, P.O. Box 5246, Raleigh, NC 27607
74. Don Ellis, Genesis Energy Systems, Div. of Hattersly & Sons, Inc., 3989 Mobil Avenue, Fort Wayne, IN 46896
75. R. J. Fiskum, Energy Conversion Equipment Branch, CE-113.2, Department of Energy, 1000 Independence Avenue S.W., Washington, DC 20585
76. Dan Folkmann, Center for Urban Community Development, Univ. of Wisconsin—Milwaukee, 929 North 6th Street, Milwaukee, WI 53203
77. Victor Goldschmidt, Ray W. Herrick Laboratories, Purdue University, W. Lafayette, IN 47907
78. E. Granryd, Dept. of Applied Thermodynamics and Refrigeration, Royal Institute of Technology, S-10044 Stockholm, Sweden
79. Robert M. Gregson, Vice President, Alten Northwest, 1134 Poplar Place, S., Seattle, WA 98144
80. G. C. Groff, Director, Research Division, Carrier Corporation, Carrier Parkway, Syracuse, NY 13201
81. Floyd Hayes, Thermal Systems, The Trane Company, 3600 Pammell Creek Road, LaCrosse, WI 54601
82. Mark R. Hogan, Manager, Westinghouse Electric Corporation, R&D Center, Purdue Industrial Res. Park, 1291 Cumberland Avenue, West Lafayette, IN 47906
83. Michael Hughes, Friedrich Air Conditioning & Refrigeration, 2007 Beechgrove Pl., Utica, NY 13507
84. Patrick J. Hughes, P.E., W. S. Fleming & Associates, Inc., 5802 Court Street Road, Syracuse, NY 13206
85. G. Hultmark, Secretary, Chalmers Univ. of Technology, Jordvarme Gruppen, S-41296, Goteborg, Sweden
86. Bao Hwang, David Taylor Naval Ship R&D Center, Mail Code 2722, Annapolis Laboratory, Annapolis, MD 21402
87. Douglas Jardine, Kaman Sciences Corporation, 1500 Garden of the Gods Rd., Colorado Springs, CO 80907
88. William S. Johnson, P.E., University of Tennessee Energy, Environment, and Resources Center, Knoxville, TN 37996-0710
89. W. A. Jury, Assoc. Professor of Soil Physics, Dept. of Soil & Environ. Sci., University of California, Riverside, CA 92521

90. Mark Kalman, Groover Eng. Co., Inc., 4258 Woodland Brook Dr., NW, Atlanta, GA 30339
91. Richard Kurtz, Naval-Base-Housing Engineering, Naval Civil Engineering Lab., Port Hueneme, CA 93043
92. Edward A. Kush, 119 Woodbury Road, Huntington, NY 11743
93. Arvo Lannus, Residential & Commercial Applications, Electric Power Research Inst., 3412 Hillview Avenue, P.O. Box 10412, Palo Alto, CA 94303
94. Terry R. Larson, Marketing Services Manager, PLEXCO, 3240 N. Manniheim Road, Franklin Park, IL 60131
95. J. H. Lehr, Executive Director, National Well Water Assoc., 500 West Wilson Bridge Road, Suite 135, Worthing, OH 43085
96. Calvin D. MacCracken, Calmac Manufacturing Company, 150 South Van Brunt Street, Englewood, NJ 07631
97. M. J. McCabe, Building Equipment Division, Department of Energy, CE-113, GH-068, 1000 Independence Avenue, S.W., Washington, DC 20585
98. Philip Metz, Brookhaven National Laboratory, Building 701, Upton, NY 11973
99. W. Calvin Moore, 360 Tri-Hill Drive, York, PA 17403
100. P. Munter, Teknologisk Institut, Gregersensvej, DK-2630 Tastrup, Denmark
101. Joseph P. Murphy, Director of Education and Training, Oasis Energy Systems, 4425 N. High Street, Columbus, OH 43214
102. Richard A. O'Neil, Niagara Mohawk Power Corporation, 300 Erie Blvd. West, Syracuse, NY 13202
103. R. E. Oliver, Department of Energy, CE-111.1, FORSTL, Washington, D.C. 20585
104. Sven G. Oskarsson, Cantherm, 8089 Trans-Canada Hwy., St. Laurent, Quebec H4S 1S4
105. Jerald Parker, School of Mechanical & Aerospace Eng., Oklahoma State University, 218 Engineer North, Stillwater, OK 74078
106. James R. Partin, GeoSystems, Inc., 3623 N. Park Drive, Stillwater, OK 74074
107. M. Porsvig, Danish Geotechnical Inst., 1 Maglebjergvej, DK-2800 Lyngby, Denmark
108. Gary G. Purcell, Electric Power Research Institute, 3412 Hillview Avenue, Palo Alto, CA 94303
109. Larry A. Raffensberger, Product Planning Manager, Borg Warner Central, Environmental Systems, P.O. Box 1592, York, PA 17405
110. Dean Rask, Honeywell Inc., 1660 South Hwy-100, St. Louis Park, MN 55416
111. J. Rizzuto, New York State Energy Research & Development Auth., Agency Building No. 2, Rockefeller Plaza, Albany, NY 12223
112. G. Rosenbald, Chalmers University of Technology, Jordvarme Gruppen, S-41296, Goteborg, Sweden
113. J. D. Ryan, Energy Conversion Equipment Branch, CE-113.2, Department of Energy, 1000 Independence Avenue S.W., Washington, DC 20585
114. Maxine Savitz, 5019 Lowell Street, N.W., Washington, DC 20016
115. Paul W. Scanlon, Manager, Engineering, Burt, Hill, Kosar, Rittelmann Assoc., 400 Morgan Circle, Butler, PA 16001
116. F. Schabkar, Graz University of Technology, Kopernikusgasse 24, A-8010 GRAZ, Austria

117. Ralph Schlichtig, P.E., Unconventional Heat and Power Sources, 11212 3rd Avenue, S., Seattle, WA 98168
118. A. H. Schroer, Sales Development Manager, Shell Chemical Company, Polybutylene Department, One Shell Plaza, P.O. Box 2463, Houston, TX 77002
119. Howard N. Shapiro, Dept. of Mech. Eng., Engineering Research Inst., Iowa State University, Ames, IA 50010
120. David N. Shaw, Shaw Engineering Associates, 1799 Farmington Ave.—Bldg. B, Unionville, CT 06085
121. Graham Siegel, TVA Chattanooga, Research & Development, 1850 Commerce Union Bank Bldg., Chattanooga, TN 37401
122. Gary Skartvedt, American Heliothermal Corporation, Denver, CO 80222
123. Mason Somerville, Professor, Dept. of Mech. Eng., University of Arkansas, Fayetteville, AR 72701
124. Mario A. Sophocleous, Kansas Geological Survey, University of Kansas, Lawrence, KS 66044
125. Don Stephenson, National Research Council, Division of Buildings Res., Montreal Road, Ottawa, Canada KIA 0R6
126. Lee Sumner, Research Engineer, York Division, Borg-Warner Corporation, P.O. Box 1592, York, PA 17405
127. O. J. Svec, Geotechnical Section, Division of Building Research, National Research Council of Canada, Ottawa, Ontario KIA OR6
128. M. Keith Swinehart, Vanguard Plastics, Inc., 831 N. Vanguard Street, McPherson, KS 67460
129. Ralph Tilney, Alco Controls, 336 Chasselle, St. Louis, MO 63141
130. S. E. Veyo, Manager, Heat Exchange Systems, Westinghouse R&D Center, 1310 Beulah Road, Pittsburgh, PA 15235
131. Warren W. Walkley, Manager, Energy Office, General Electric Co., 777 14th Street, NW, Washington, DC 20005
132. Michael R. Warfel, Senior Scientist, Geraghty & Miller, Inc., 6800 Jericho Turnpike, Syosset, NY 11791
133. Jeffrey W. Wright, Engineering Consultant, Kansas Gas and Electric Co., Wichita, KS
134. Office of the Assistant Manager for Energy R&D, U.S. Department of Energy, Oak Ridge Operations, Oak Ridge, TN 37831

135–161. Technical Information Center, Department of Energy, P.O. Box 62, Oak Ridge, TN 37831